

CARS: the CFHTLS-Archive-Research Survey

I. Five-band multi-colour data from 37 sq. deg. CFHTLS-wide observations^{*}

T. Erben¹, H. Hildebrandt^{2,1}, M. Lerchster^{3,4}, P. Hudelot^{1,6}, J. Benjamin⁵, L. van Waerbeke⁵, T. Schrabback^{2,1},
F. Brimiouille³, O. Cordes¹, J. P. Dietrich⁷, K. Holhjem¹, M. Schirmer¹, and P. Schneider¹

¹ Argelander-Institut für Astronomie, University of Bonn, Auf dem Hügel 71, 53121 Bonn, Germany
e-mail: terben@astro.uni-bonn.de

² Sterrewacht Leiden, Leiden University, Niels Bohrweg 2, 2333 CA Leiden, The Netherlands

³ University Observatory Munich, Department of Physics, Ludwigs-Maximilians University Munich, Scheinerstr. 1, 81679 Munich, Germany

⁴ Max-Planck-Institut für extraterrestrische Physik, Giessenbachstraße, 85748 Garching, Germany

⁵ Department of Physics and Astronomy, University of British Columbia, Vancouver, BC V6T 1Z1, Canada

⁶ Institut d'Astrophysique de Paris, 98bis bd. Arago, 75014 Paris, France

⁷ ESO, Karl-Schwarzschild-Strasse 2, 85748 Garching, Germany

Received 19 June 2008 / Accepted 7 November 2008

ABSTRACT

Context. We present the CFHTLS-Archive-Research Survey (CARS). It is a virtual multi-colour survey that is based on public archive images from the Deep and Wide components of the CFHT-Legacy-Survey (CFHTLS). Our main scientific interests in the CFHTLS Wide-part of CARS are optical searches for galaxy clusters from low to high redshift and their subsequent study with photometric and weak-gravitational lensing techniques.

Aims. As a first step in the CARS project, we present multi-colour catalogues from 37 sq. degrees of the CFHTLS-Wide component. Our aims are first to create astrometrically and photometrically well-calibrated co-added images from publicly available CFHTLS data. Second, we offer five-band ($u^*g'r'i'z'$) multi-band catalogues with an emphasis on reliable estimates for object colours. These are subsequently used for photometric redshift estimates.

Methods. We consider all those CFHTLS-Wide survey pointings that were publicly available on January 2008 and that also have five-band coverage in $u^*g'r'i'z'$. The data were calibrated and processed with our GaBoDS/THELI image processing pipeline. The quality of the resulting images was thoroughly checked against the Sloan-Digital-Sky Survey (SDSS) and already public high-end CFHTLS data products. From the co-added images we extracted source catalogues and determined photometric redshifts using the public code Bayesian Photometric Redshifts (BPZ). Fifteen of our survey fields directly overlap with public spectra from the VIMOS VLT deep (VVDS), DEEP2 and SDSS redshift surveys, which we used for calibration and verification of our redshift estimates. Furthermore we applied a novel technique, based on studies of the angular galaxy cross-correlation function, to quantify the reliability of photo- z 's.

Results. With this paper we present 37 sq. degrees of homogeneous and high-quality five-colour photometric data from the CFHTLS-Wide survey. The median seeing of our data is better than 0.9 in all bands and our catalogues reach a 5σ limiting magnitude of about $i'_{AB} \approx 24.5$. Comparisons with the SDSS indicate that most of our survey fields are photometrically calibrated to an accuracy of 0.04 mag or better. This allows us to derive photometric redshifts of homogeneous quality over the whole survey area. The accuracy of our high-confidence photo- z sample (10–15 galaxies per sq. arcmin) is estimated with external spectroscopic data to $\sigma_{\Delta_z/(1+z)} \approx 0.04$ – 0.05 up to $i'_{AB} < 24$ with typically only 1–3% outliers. In the spirit of the Legacy Survey we make our catalogues available to the astronomical community. Our products consist of multi-colour catalogues and supplementary information, such as image masks and JPEG files to visually inspect our catalogues. Interested users can obtain the data by request to the authors.

Key words. surveys – galaxies: photometry

1. Introduction

Being the signposts of the largest density peaks of the cosmic matter distribution, clusters of galaxies are of particular interest for cosmology. The statistical distribution of clusters as a

function of mass and redshift forms one of the key cosmological probes. Since their dynamical or evolutionary timescale is not much shorter than the Hubble time, they contain a “memory” of the initial conditions for structure formation (e.g. [Borgani & Guzzo 2001](#)). The population of clusters evolves with redshift, and this evolution depends on the cosmological model (e.g. [Eke et al. 1996](#)). Therefore, the redshift dependence of the cluster abundance has been used as a cosmological test (e.g. [Bahcall & Fan 1998](#); [Borgani et al. 1999](#); [Schuecker et al. 2003a,b](#)). A prerequisite for these studies are large and homogeneous cluster samples with well-understood selection functions. Consequently, a wide variety of systematic searches have been performed in various parts of the electromagnetic spectrum. The most extensive cluster searches and cosmological studies were

^{*} Based on observations obtained with MegaPrime/MegaCam, a joint project of CFHT and CEA/DAPNIA, at the Canada-France-Hawaii Telescope (CFHT), which is operated by the National Research Council (NRC) of Canada, the Institut National des Sciences de l'Univers of the Centre National de la Recherche Scientifique (CNRS) of France, and the University of Hawaii. This work is based in part on data products produced at TERAPIX and the Canadian Astronomy Data Centre (CADC) as part of the Canada-France-Hawaii Telescope Legacy Survey, a collaborative project of NRC and CNRS.

performed in X-rays (see e.g. Böhringer et al. 2000; Reiprich & Böhringer 2002; Böhringer et al. 2004; Mantz et al. 2008) and in the optical (see e.g. Postman et al. 1996; Olsen et al. 1999; Gladders & Yee 2000; Goto et al. 2002; Bahcall et al. 2003; Gladders et al. 2007; Koester et al. 2007); see also Gal (2008) for a concise review of various cluster detection algorithms in the optical. Each of the cluster searches relies on certain cluster properties such as X-ray emission of the hot intra-cluster gas or an optical overdensity of red galaxies and may introduce systematic biases in the candidate list creation. Hence, a careful comparison and selection with different methods on the same area of the sky is essential to obtain a comprehensive understanding of galaxy clusters and their mass properties.

The Wide part of the Canada-France-Hawaii-Telescope Legacy Survey (CFHTLS-Wide) is an optical Wide-Field-Imaging-Survey particularly well suited for such studies. When completed it will cover 170 sq. deg. in the five optical Sloan filters $u^*g'r'i'z'$ to a limiting magnitude of $i'_{AB} \approx 24.5$. The unique combination of area, depth and wavelength coverage allows the application of a variety of currently available optical search algorithms. For instance, the Postman matched filter technique (see Postman et al. 1996) applies an overdensity and luminosity function filter to photometric data of a single band survey. It can provide high-confidence samples in the low- and medium redshift range (see e.g. Olsen et al. 1999, 2001). The Red-Cluster-Sequence algorithm scans a two-filter survey for the Red Sequence of elliptical galaxies and is mainly used for the medium to high redshift regime with the r and z filters (Gladders & Yee 2000). The existence of five bands in the CFHTLS-Wide allows us to estimate photometric redshifts and the application of techniques using distance information (e.g. Miller et al. 2005). Furthermore, one of the main goals of the CFHTLS-Wide are weak gravitational lensing studies of the large-scale structure distribution (see e.g. Hoekstra et al. 2006; Fu et al. 2008, for recent results). This will allow us to complement and to directly compare optical cluster searches with candidates from weak lensing mass reconstructions and shear peak detections (see e.g. Schneider 1996; Erben et al. 2000; Bartelmann & Schneider 2001; Wittman et al. 2001, 2003; Dahle et al. 2003; Hettterscheidt et al. 2005; Wittman et al. 2006; Schirmer et al. 2007; Dietrich et al. 2007). To perform these galaxy cluster studies, we perform an extensive Archive-Research programme on publicly available data from the CFHTLS-Wide. We baptise our survey the CFHTLS-Archive-Research Survey (CARS in the following).

This paper marks the first step of our science programme on a significant area of CARS. We describe our data handling and the creation of multi-colour catalogues, including a first set of photometric redshifts, on 37 sq. degrees of five-colour CARS data.

The article is organised as follows: Sect. 2 gives a short overview on our current data set; a detailed description of our complete image data handling is given in Appendix A. Sections 3 and 4 summarise the multi-colour catalogue creation and the photometric redshift estimation together with a thorough quantification of their quality. We continue to describe our data products (Sect. 5) and finish with our conclusions in Sect. 6.

2. The data

The current set of CARS data consists of a subset of the synoptic CFHTLS-Wide observations which is one of three independent parts of the Canada-France-Hawaii-Telescope Legacy Survey (CFHTLS). It is a very large, 5-year project designed

and executed jointly by the Canadian and French communities. The survey started in spring 2003 and is planned to finish during 2008. All observations are carried out with the MegaPrime instrument mounted at the Canada-France-Hawaii Telescope (CFHT). MegaPrime (see e.g. Boulade et al. 2003) is an optical multi-chip instrument with a 9×4 CCD array (2048×4096 pixel in each CCD; $0'.186$ pixel scale; $\approx 1^\circ \times 1^\circ$ total field-of-view). When completed, the CFHTLS-Wide will cover 170 sq. deg. in four high-galactic-latitude patches W1–W4 of 25 to 72 square degrees through the five optical filters $u^*g'r'i'z'$ down to a magnitude of $i'_{AB} \approx 24.5$. See <http://www.cfht.hawaii.edu/Science/CFHLS/> and <http://terapix.iap.fr/cplt/oldSite/Descart/summarycfhtlswide.html> for further information on survey goals and survey implementation.

Since June 2006 CFHTLS observations are publicly released to the astronomical community via the Canadian Astronomy Data Centre (CADC)¹. At the time of writing raw and Elixir preprocessed images (see below), together with auxiliary metadata, can be obtained 13 months after observations.

For the current work we consider all Elixir processed CFHTLS-Wide fields with observations in all five optical colours $u^*g'r'i'z'$ which were publicly available on 18/01/2008, i.e. observed until 18/12/2006. In total, the current CARS set consists of 37 sq. degrees split between the three CFHTLS-Wide patches W1 (21 sq. degrees), W3 (five sq. degrees) and W4 (eleven sq. degrees). The areas around the defined patch centres (W1: RA = 02:18:00, Dec = -07:00:00, W3: RA = 14:17:54, Dec = +54:30:31 and W4: RA = 22:13:18, Dec = +01:19:00) are covered on a regular grid with pointed observations. Names of individual CARS pointings are constructed like W1m1p2 (read “W1 minus 1 plus 2”; see also Fig. 1). They indicate the patch and the separation (approximately in degrees) from the patch centre, e.g. pointing W1m1p2 is about one degree west and two degrees north from the W1 centre. The overlap of adjacent pointings is about 3'0 in RA and 6'0 in Dec. The exact layout of the CARS survey fields is shown in Fig. 1. All three patches are covered by spectroscopic surveys which allow us to calibrate and to verify photometric redshift estimates later on; W1 and W4 overlap with the VIMOS VLT Deep Survey (VVDS; see Le Fèvre et al. 2005; Garilli et al. 2008), W3 with the DEEP2 galaxy redshift survey (see Davis et al. 2007). Moreover, CARS data from patches W3 and W4 have complete overlap with the Sloan-Digital-Sky-Survey (SDSS; see e.g. Adelman-McCarthy et al. 2007). From patch W1 only the southern pointings W1p3m0, W1p4m0 and W1p1m1 have SDSS overlap.

The Elixir data preprocessing performed at CFHT (see Magnier & Cuillandre 2004) includes removal of the instrumental signature from raw data (bias/dark subtraction; flat-fielding; fringe correction in i' and z' data) and absolute photometric calibration (determination of zeropoints, colour terms and extinction coefficients, corrections for scattered light effects which lead to significant inhomogeneous photometric zeropoints across the CCD mosaic, see e.g. Manfroid et al. 2001; Koch et al. 2004; Regnault 2007). The data is accompanied with comprehensive information on the observing conditions (seeing, sky-transparency, sky-background level) for each exposure².

After downloading all data from CADC and rejecting exposures with a problematic CFHT quality assessment we further process the data on a pointing/colour basis with our

¹ See <http://www1.cadc-ccda.hia-ihc.nrc-cnrc.gc.ca/cadc/>

² See <http://www.cfht.hawaii.edu/Science/CFHTLS-DATA/exposurescatalogs.html>

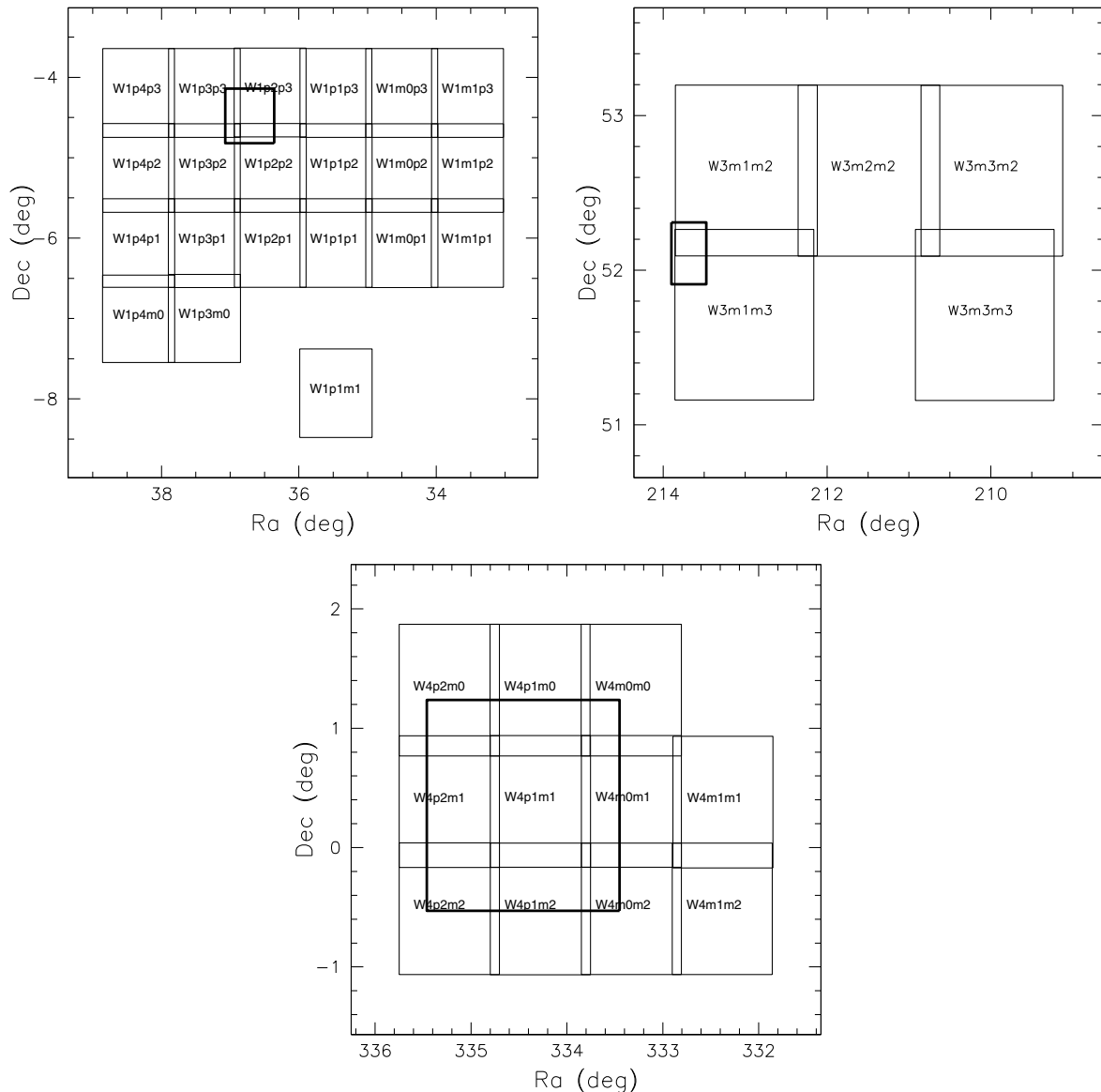


Fig. 1. Layouts of the current three CARS: the CARS data of this work are split up in the three CFHTLS-Wide patches W1 (21 sq. degrees; patch centre: RA = 02:18:00, Dec = $-07:00:00$), W3 (five sq. degrees; patch centre: RA = 14:17:54, Dec = $+54:30:31$) and W4 (11 sq. degrees; patch centre: RA = 22:13:18, Dec = $+01:19:00$). In areas covered by thick lines spectra from various surveys are publicly available for photo- z calibration and verification (see text for details).

GaBoDS/THELI pipeline to produce deep co-added images for scientific exploitation. Our algorithms and software modules to process multi-chip cameras are described in Erben et al. (2005) and most of the details do not need to be repeated here. For the interested reader we give in Appendix A a thorough description of the CARS data handling, data peculiarities and the pipeline upgrades/extensions necessary to smoothly and automatically process MegaPrime data. In addition, a comprehensive assessment of the astrometric and photometric quality of our data, together with a comparison to previous releases of CFHTLS data can be found there. We conclude that the CARS data set is accurately astrometrically and photometrically calibrated for multi-colour photometric and lensing studies.

In the following we give a very brief summary of the most important CARS data characteristics: the first products of the THELI processing are 185 co-added science images accompanied by weight maps which characterise their noise properties (see e.g. Sect. 6 of Erben et al. 2005, for a discussion on the role

of weight images in the object detection process). Our image stacking procedure first automatically identifies image defects (hot and cold pixel, cosmic ray hits and satellite tracks) in the individual frames and assigns them zero weight in the co-addition process. The stacking itself is a statistically optimal, weighted mean co-addition taking into account sky background variations and photometric zeropoint variations in the individual frames (see Sects. 6 and 7 from Erben et al. 2005 and Appendix A for further details). Identifying and masking image defects in the individual images before co-addition allows us to obtain clean stacked images also if only very few input images are contributing. This is essential for the processing of CARS r' -band data where most pointings are covered only by two individual exposures. As an example, we show in Fig. 2 the final co-added r' -band image of the field W1p3p1. We perform numerous internal and external tests to quantify the astrometric and photometric properties of our data. In Appendix A.3 we conclude that the internal astrometric accuracy of our data, i.e. the accuracy with

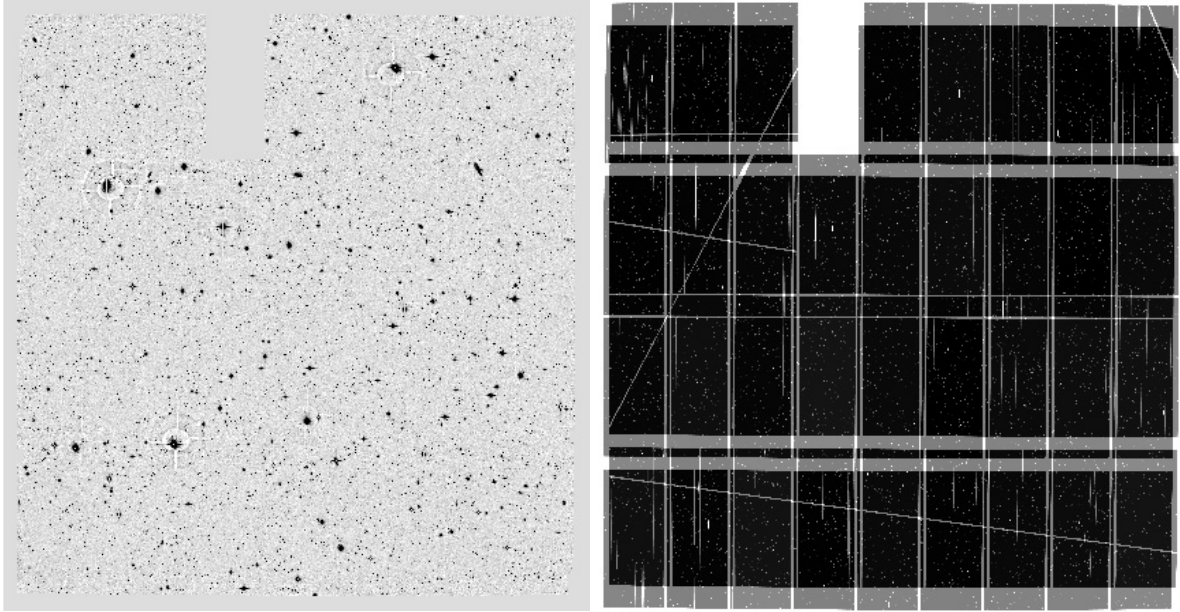


Fig. 2. Co-added CARS data: We show the final science image of the r' -band observations from field W1p3p1 (*left panel*) and the accompanying weight map (*right panel*). The weight map shows five extended satellite tracks which were automatically identified and masked before image co-addition (see Appendix A.2 for details). In several CARS pointings/colours individual chips did not contain useful data and were hence excluded from the analysis. The pointing shown suffered from this problem in the uppermost row.

which we can align individual exposures of a colour and pointing, is $0'.03$ – $0'.04$ (1/5th of a MegaPrime pixel) over the whole field-of-view of MegaPrime; our absolute astrometric frame is given by the USNO–B1 catalogue (see Monet et al. 2003). The co-added images of the different colours from each pointing are aligned to sub-pixel precision in all cases.

We quantify the quality of the photometric calibration of our data in Appendices A.4, A.6 and A.7. First, we investigate photometric flatness over the MegaPrime field-of-view. We use data from the CFHTLS-Deep survey which keeps observing four sq. degrees over the whole five-year period of the CFHT-Legacy Survey. This allows us to create image stacks from different epochs and to investigate photometric consistency. Magnitude comparisons of co-additions obtained from the three years 2003, 2004 and 2005 indicate uniform photometric properties with a dispersion of $\sigma_{\text{int},u^*g'r'i'} \approx 0.01$ – 0.02 mag in $u^*g'r'i'$ and about $\sigma_{\text{int},z'} \approx 0.03$ – 0.04 mag in z' . We attribute higher residuals in z' to fringe residuals in this band.

Our absolute magnitude zeropoints are tested against photometry in the SDSS and against previous data releases of the CFHTLS. Our comparison with the SDSS shows that our absolute photometric calibration agrees with Sloan to $\sigma_{\text{abs},g'r'i'} \approx 0.01$ – 0.04 mag in $g'r'i'$ and $\sigma_{\text{abs},z'} \approx 0.03$ – 0.05 mag for z' . While the calibration in these four bands seems to be unbiased, we observe, at the current stage, a systematic magnitude offset in u^* of about 0.1 mag with respect to Sloan (CARS magnitudes appear fainter than Sloan). For u^* -band data from spring to fall 2006 our analysis suggests an Elixir calibration problem leading to offsets of 0.2–0.3 mag in u^* .

Finally, we directly compared our flux measurements with those of the previous CFHTLS TERAPIX T0003 release and Stephen Gwyn’s MegaPipe project (see Gwyn 2008). The measurements to T0003 are in very good agreement with typical dispersions of 0.02 mag; in many cases larger scatters are observed with respect to the MegaPipe data. Private communication with Gwyn suggests that several MegaPipe stacks suffer from the accidental inclusion of images obtained under unfavourable

Table 1. Characteristics of the CARS co-added science data with basic average properties of our final science data (see text for an explanation of the columns).

Filter	expos. time [s]	m_{lim} [AB mag]	seeing ["]
u^* (<i>u.MP9301</i>)	5×600 (3000)	25.24	0.87
g' (<i>g.MP9401</i>)	5×500 (2500)	25.30	0.85
r' (<i>r.MP9601</i>)	2×500 (1000)	24.36	0.79
i' (<i>i.MP9701</i>)	7×615 (4305)	24.68	0.71
z' (<i>z.MP9801</i>)	6×600 (3600)	23.20	0.66

photometric conditions; see Appendices A.7 and A.8 for further details.

Table 1 lists average properties for seeing and limiting magnitude values in our survey data. The quoted values for exposure time (we list the typical exposure time per dither, the number of dithered observations per colour and the total exposure time in parentheses), limiting magnitudes and seeing correspond to a typical field and hence give a good indication of what can be expected from the data. The seeing values (SExtractor parameter FWHM_IMAGE for stellar sources) are the median of measured seeing values from all co-added science images in the corresponding filters. We note that we measure a seeing of $1''.0$ or below for all co-added CARS stacks except for the u^* -band image of W1p3p3 for which we obtain $1''.1$. The limiting magnitude is defined as the $5\text{-}\sigma$ detection limit in a $2''.0$ aperture via $m_{\text{lim}} = ZP - 2.5 \log(5 \sqrt{N_{\text{pix}}} \sigma_{\text{sky}})$, where ZP is the magnitude zeropoint, N_{pix} is the number of pixels in a circle with radius $2''.0$ and σ_{sky} the sky background noise variation. The actual numbers for m_{lim} in Table 1 were obtained from the field W4p2m0. It represents a CARS pointing with typical properties concerning exposure times and image seeing. A more detailed table listing these quantities for each individual field can be found in Appendix A.9.

The described imaging data form the basis for the subsequent multi-colour catalogue creation and photo- z estimation.

3. The multi-colour catalogues

Our procedures to create multi-colour catalogues for the five-band CARS data are similar to the ones presented in [Hildebrandt et al. \(2006\)](#) where we studied Lyman-break galaxies in the ESO Deep Public Survey (DPS).

3.1. Preparation and PSF equalisation

In order to estimate unbiased colours it is necessary to measure object fluxes in the same physical apertures in each band, i.e. for a given object the same physical parts of the object should be measured in the different bands. Since the PSF usually varies from band to band we apply a convolution to degrade the seeing of all images of one field to the PSF size of the image with the worst seeing. Assuming a Gaussian PSF we first measure the seeing and then calculate appropriate filter functions by the following formula:

$$\sigma_{\text{filter},k} = \sqrt{\sigma_{\text{worst}}^2 - \sigma_k^2}, \quad (1)$$

with $\sigma_{\text{filter},k}$ being the width of the Gaussian filter for convolution of the k th image, σ_{worst} being the PSF size of the image with the worst seeing, and σ_k being the PSF size of the k th image. By doing so we neglect the non-Gaussianity of a typical ground-based PSF. Nevertheless, experience with the DPS shows that our procedure is sufficient to estimate reliable colours if the seeing values in the individual colours are subarcsecond and not too different. In CARS, the seeing values for a pointing typically do not differ by more than $0''.2$ – $0''.3$ (see [Table A.2](#)).

3.2. Limiting magnitudes

The images filtered in that way are then analysed for their sky-background properties. For the accurate estimation of photometric redshifts it is important to have a reasonable estimate for the limiting magnitude at a given object position. Therefore, we create limiting magnitude maps from the rms fluctuations of the sky-background in small parts of the image. Here we use 1σ limiting magnitudes calculated in a circular aperture of $2\times$ stellar FWHM diameter. This procedure ensures that varying depths over the field are properly taken into account in the colour estimation. It may well be that an object would be detected in one part of the image whereas it is undetectable in a different part due to the dither pattern or stray-light leading to inhomogeneous depth. By assigning position-dependent limiting magnitudes to each object in all bands we can later decide which flux measurements are significant and which are not.

3.3. Object detection

The object detection is performed with SExtractor (see [Bertin & Arnouts 1996](#)) in dual-image mode and we consider all objects having at least 5 connected pixels exceeding 2σ of the sky-background variation. We will base our primary science analyses (galaxy cluster searches and weak lensing applications) on the i' -band data. Hence, we generate our object catalogues based on this colour rather than on a combination of all available colours such as a χ^2 image (see e.g. [McCracken et al. 2003](#)). We use the unconvolved i' -band image as the detection image and measure fluxes for the colour estimation and the photometric redshifts on the convolved frames. Colour indices are estimated from the differences of isophotal magnitudes taking into account local limiting magnitudes, i.e. if a magnitude is measured to be fainter

than the local limiting magnitude, then this limit is used instead of the measured magnitude to estimate an upper/lower bound for the colour index.

Additionally, we also measure the total i' -band magnitudes on the unconvolved image so that total magnitudes in the other bands can in principle be calculated from those and from the colour indices. However, it should be noted that our approach to run SExtractor in dual-image-mode with the unconvolved i' -band image for detection will never lead to accurate total magnitudes in the $u^*g'r'z'$ -bands. While adding/subtracting the appropriate colour index to/from the total i' -band magnitude yields accurate total magnitudes in one of the other bands for bright objects without a colour gradient, it can yield strongly biased results in other cases. Only catalogues created in single-image-mode on the different bands assure a reliable estimation of total magnitudes. Since our emphasis here is on estimating colours as accurately as possible, we do not pursue this issue further.

3.4. Creation of image masks

All CARS pointings suffer from bright stars and other large- and small-scale astronomical features that we would like to exclude from the following analysis. At least we want to know the location and shape of those areas so that catalogues can be cleaned from objects in problematic areas. Of course the regions which need to be masked heavily depend on the science project for which our data are used. Our main scientific drivers for the CARS data are the photometric identification of galaxy-clusters and their subsequent investigation with photometric redshift and weak gravitational lensing techniques. These applications require the accurate determination of galaxy surface brightness moments to at least fourth order. Hence, we want to exclude all image areas in which the light distribution of faint objects (often confined to a very small number of image pixels) is probably altered by other sources. Amongst such defects are:

- extended haloes of very bright stars;
- diffraction spikes of stars;
- areas around very large galaxies;
- various kinds of image reflections;
- tracks of asteroids.

A complete manual masking process for the large amount of CARS data would be a prohibitively long and man-power intensive task. We developed a software package which generates template masks for most image features which we want to reject. If necessary, these automatically generated masks are manually optimised later. Our tools are based on the following ideas:

1. Object detection algorithms such as SExtractor identify astronomical sources by connected areas which exceed the sky background noise by a certain amount. The pixel distribution of THELI produced images of *empty* fields has mode zero after sky subtraction. Large-scale artefacts like stellar reflection rings lead to local deviations of the background. By running SExtractor with a fixed background value of zero and a very low detection threshold of 0.6σ , this local variation of the background leads to a significant increase in the detection of spurious objects. We examine the SExtractor catalogue for areas of significant over-densities and strong gradients in the object density distribution. Corresponding image regions are flagged as problematic. The output of the procedure is an 8-bit FITS FLAG image with the size of the original image (masked areas are “1” and unmasked areas are “0” in this image) or/and

a saoiimage/ds9 polygon region file of masked areas. See [Dietrich et al. \(2007\)](#) for further details on the algorithm and its implementation.

2. Astronomical Standard Star Catalogues such as USNO-B1, GSC-2 or SDSS-R5 list the positions and magnitudes of known astronomical sources up to a magnitude of about 18. In the CARS data, the large majority of these objects with $m \leq 16$ are bright or moderately bright stars whose surroundings should be excluded from object catalogues (faint haloes, diffraction spikes). Moreover, stellar sources have well defined shapes over the complete MegaPrime field-of-view. The extent of the central light concentration and the width and the height of stellar diffraction spikes can be modelled as function of apparent magnitude. On the basis of these observations we automatically create object masks for stellar objects:
 - We retrieve object positions and magnitudes from the Standard Star Catalogues GSC-1, GSC-2.3.2 and USNO-A2. We found that our selection criteria in these catalogues (magnitude limits, catalogue flags) result in slightly different source lists and hence the three samples complement each other. Our masking is performed independently on all three catalogues.
 - At each catalogue position we lay down template masks for the central light halo and the diffraction spikes. The templates are scaled with (red photographic) magnitude to conservatively encompass the stellar areas. In addition, for very bright stars with $m < 10.35$ we mask extended stellar diffraction haloes. For MegaPrime these haloes have an extend of about 4.0 depending only weakly on magnitude. Moreover, these haloes occur with a radial offset towards the MegaPrime centre. The halo displacement from the stellar centre as function of MegaPrime position can well be described by -0.022 times the relative position of the star with respect to the camera centre.
 - Finally, the masks are converted to saoiimage/ds9 polygon region files which can further be processed by the WeightWatcher programme (see [Bertin & Marmo 2007](#); [Marmo & Bertin 2008](#)) to construct a FLAG_IMAGE file.
3. Tracks of fast moving asteroids typically show up as a series of high S/N, lined up, short dashed and highly elliptical objects in co-added CARS images. They are present in the data because our strictly linear co-addition process does not include any pixel rejection/clipping procedure. We try to detect and mask them in our multi-colour object catalogues. We identify an asteroid candidate if a minimum number of N objects are located within 0.4 pixels from a line connecting any two objects within overlapping boxes of $M \times M$ pixels². We run this algorithm for the two parameter sets $N = 4$; $M = 100$ and $N = 5$; $M = 175$ and merge the resulting candidate lists. This combination was found empirically to give good results on the CARS data set. For real asteroids the ellipticities of contributing objects are usually highly aligned. As in weak lensing theory (see e.g. [Bartelmann & Schneider 2001](#)) we compute the two-component ellipticity

$$(\epsilon_1, \epsilon_2) = \frac{1-r}{1+r} (\cos 2\theta, \sin 2\theta), \quad (2)$$

which depends on the object axis ratio r and position angle θ as determined by SExtractor. The expectation value of both ellipticity components is zero if the ellipticities of

different objects are not aligned. We then compute the alignment estimator

$$A = \sqrt{[\text{median}(\epsilon_1)]^2 + [\text{median}(\epsilon_2)]^2} \quad (3)$$

from the ellipticities of all objects belonging to a candidate. We only keep asteroid candidates with $A > 0.20$; $A > 0.24$ (first and second parameter set) in order to minimise the false flagging of galaxies in areas with increased object number density, such as galaxy clusters. These parameters were optimised for typical CARS seeing conditions and image depths. For the W4m0m0 field the algorithm automatically masks 30 out of 32 visually identified asteroid tracks, with one false positive, for an object number density of 35/arcmin².

We note that the different algorithms are complementary to each other. While large-scale features such as very large galaxies or image borders influence the object density, small scale defects from medium bright stars (diffraction spikes; outer extended haloes) are caught by masking known catalogue sources. We independently run the object density analysis on all five colours of a CARS pointing. However, the stellar and asteroid track masks are calculated for the i' -band only. The latter ones need some manual revision which is done on the basis of the i' -band image only. Hence, asteroid tracks in the $u^*g'r'z'$ bands are not included in our object masks. Other problems which require manual optimisation of the image masks are: (1) the object density distribution analysis also masks rich galaxy clusters. (2) Some objects labelled as stellar source in the Standard Star Catalogues are galaxies. (3) For images with an exceptional good seeing of 0.6 or better the high density of objects leads to a significant number of false positives in the asteroid masking. The final masks from the individual colours are merged and collected in one saoiimage/ds9 polygon region file. The masking information is also transferred to our multi-colour catalogues as a MASK key which allows an easy filtering of problematic sources later. Figure 3 shows examples of our masking procedure.

4. Photometric redshifts

From the multi-colour catalogues described in the preceding section we estimate photometric redshifts for all objects in two steps. In a first pass we use available spectroscopic information from the VVDS³ to *correct/recalibrate* our photometric zero-points on a patch-wide basis. Afterwards we obtain photo- z estimates for our objects (see [Hildebrandt et al. 2008](#)). In the following we set the minimal photometric error to 0.1 mag in order to avoid very small purely statistical errors for high-S/N objects and to take into account our estimated internal and external photometric accuracies (see Sect. A.8). Throughout this work we use MegaPrime filter response curves which were computed by Mathias Schultheis and Nicolas Regnault. They are available at <http://terapix.iap.fr/forum/showthread.php?tid=1364>.

The following analysis only includes secure VVDS objects (marked by flags 3, 4, 23 and 24; in total these are 4463 objects for W1 (up to a limiting magnitude of $i'_{AB} \approx 24$) and

³ Spectroscopic data were obtained from <http://cencosw.oamp.fr/VVDS/>

⁴ Note that there are at least two more sets of MegaPrime filter curves available on the WWW: On the CFHT web pages (<http://www.cfht.hawaii.edu/Instruments/Filters/megaprime.html>) and on Stephen Gwyn MegaPipe pages (<http://www1.cadc-ccda.hia-ihp.nrc-cnrc.gc.ca/megapipe/docs/filters.html>)

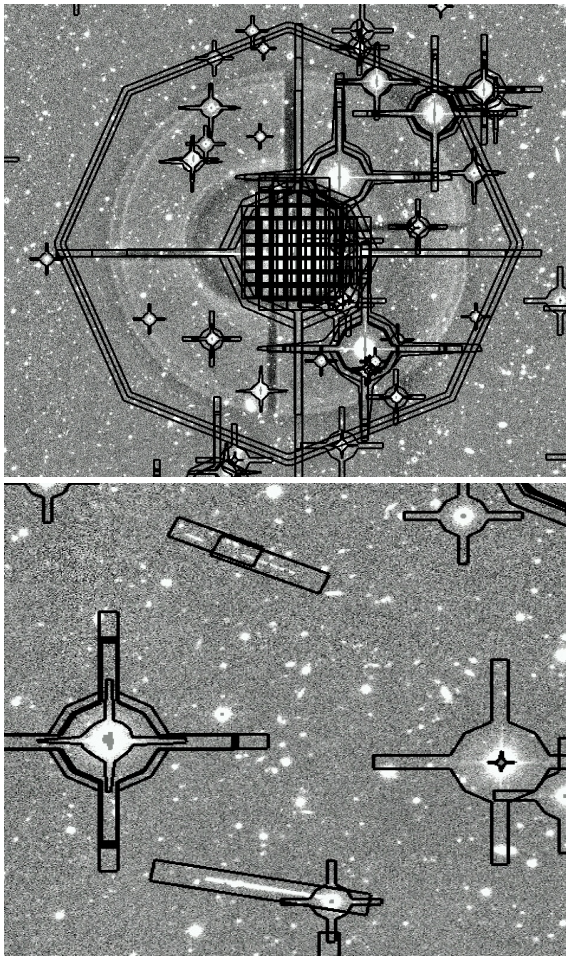


Fig. 3. Semi-automatic image masking: shown is the result of our semi-automatic image masking for areas of the field W4m0m0. The polygon squares result from our object density analysis and the stars cover sources identified in the GSC-1, GSC-2.3.2 and USNO-A2 Standard Star Catalogues (*upper panel*; multiple masks around stars appear for sources identified in various catalogues). *The lower panel* shows results from our asteroid masking procedure.

9617 for W4 (up to $i'_{AB} \approx 22.5$). Here and in the following we match objects from our source lists with those from external catalogues if their position agrees to better than $1''.0$. First we run the new version of Hyperz (Bolzonella et al. 2000)⁵ on 13 fields with overlap to the VVDS⁶, four of which are in W1 and nine in W4. We use the CWW template set (Coleman et al. 1980) supplied by Hyperz and add two starburst templates from Kinney et al. (1996). Additionally, we fix the redshift to the spectroscopic redshift for every object. In this way we find the best fitting template at the spectroscopic redshift for every object. Hyperz puts out the magnitudes of the best-fit templates and enables us to compare these to our original estimates. We average the differences between the observed and the best-fit template's magnitudes over all objects. In this way we derive corrections for the zeropoints in the five bands. We only use spectra of galaxies with $i'_{AB} \leq 21.5$ which have a high S/N photometric measurement in all filter bands; these were 654 sources in W1 and 2158 objects in W4. The mean and the

scatter of the corrections in the four W1 fields are $\Delta u^* = -0.064 \pm 0.015$ mag, $\Delta g' = 0.069 \pm 0.005$ mag, $\Delta r' = 0.027 \pm 0.019$ mag, $\Delta i' = -0.004 \pm 0.018$ mag, and $\Delta z' = 0.007 \pm 0.007$ mag. In the nine W4 fields we find $\Delta u^* = -0.088 \pm 0.011$ mag, $\Delta g' = 0.136 \pm 0.029$ mag, $\Delta r' = 0.019 \pm 0.03$ mag, $\Delta i' = 0.008 \pm 0.023$ mag, and $\Delta z' = -0.010 \pm 0.014$ mag. Note that the photo- z code is only sensitive to colours so that the absolute values of the corrections in the different bands should not be misunderstood as pure calibration errors. Prior to the calibration step, we did not modify the W3 and W4 u^* zeropoints for identified systematic calibration problems (see Appendix A.4). As all W3 and W4 fields are equally affected by it we expect that it is taken into account properly by our correction procedure. We also did not apply any galactic extinction corrections to our catalogues.

For the W1 fields that do not overlap with the VVDS we use the zeropoint corrections from the field W1p2p3, the one with the highest density of spectroscopic redshifts in the W1 region. Since the regions W3 and W4 show different u^* -band calibration systematics than W1 (see Sect. A.6), we correct all W3 fields and the two W4 fields without VVDS overlap with the values from W4p1m1, again the most densely covered field in this region.

Then we run Bayesian Photometric Redshifts (BPZ; see Benitez 2000)⁷ on the catalogues with the corrected photometry using the same template set as before. The Bayesian approach of BPZ combines spectral template χ^2 minimisation with a redshift/magnitude prior. The prior was calibrated from HDF-N observations and the Canada-France Redshift Survey (see Lilly et al. 1995). It contains the probability of a galaxy having redshift z and spectral type T given its apparent magnitude m . A detailed description of the code and the prior can be found in Benitez (2000). We restrict the fitting of the photo- z 's to $z \leq 3.9$ due to the limited depth of the Wide data. The Bayesian redshift estimates are added to our multi-colour catalogues. Note that not all objects in our catalogues have well determined photometric measurements in the full u^* to z' wavelength coverage. This can have physical reasons (e.g. high-redshift dropout galaxies which are fainter than the magnitude limit in blue passbands) or it can be connected to problems in the data itself (e.g. pixels without information in one of the filter bands). Our current catalogues miss information to cleanly distinguish between these cases but only allow us to identify problematic photometry by either large photometric errors or a flux measurement below the formal detection limit. In all cases with a magnitude estimate below the limiting magnitude, or a magnitude error larger than 1 mag, we configured BPZ to treat the object as non-detected with a flux error equal to the 1σ limiting magnitude. This leads to unreliable results if the large photometric error results e.g. from image defects and not from intrinsic source properties. To allow an easy rejection of such problematic sources each object in our catalogues obtains photometry quality flags for all filter bands.

The internal accuracy of the BPZ photo- z 's is described by the ODDS parameter (see e.g. Mobasher et al. 2004) assigning a probability to the Bayesian redshift estimate by integrating the posterior probability distribution in an interval that corresponds to the 95% confidence interval for a single-peaked Gaussian. By rejecting the most unsecure objects with a low ODDS value one can obtain much cleaner subsamples; see also Hildebrandt et al. (2008).

If not stated otherwise we use in quality assessments of our BPZ photo- z 's the following subsample of our catalogue data:

1. we reject all objects falling within an object mask (see Sect. 3.4);

⁵ Publicly available at <http://www.ast.obs-mip.fr/users/roser/hyperz/>

⁶ Spectroscopic data were obtained from <http://cencosw.oamp.fr/>

⁷ Publicly available at <http://acs.pha.jhu.edu/~txitxo/>

Table 2. Statistics of the comparison between photometric and spectroscopic VVDS redshifts.

Field	m_{lim} [AB]	N^a [%]	compl. ^b	outl. rate η^c [%]	$\Delta z/(1+z)^d$
W1p2p2	22.5	212	91.51	1.03	0.000 ± 0.052
	24.0	517	73.11	1.85	-0.002 ± 0.050
W1p2p3	22.5	1136	92.52	0.86	-0.008 ± 0.051
	24.0	2456	77.69	1.62	-0.011 ± 0.049
W1p3p2	22.5	14	92.86	0.00	0.009 ± 0.040
	24.0	24	70.83	0.00	0.011 ± 0.047
W1p3p3	22.5	104	87.50	2.20	0.004 ± 0.046
	24.0	257	65.37	1.79	0.009 ± 0.050
W4m0m0	22.5	223	93.27	1.44	-0.015 ± 0.045
W4m0m1	22.5	354	94.63	2.69	0.004 ± 0.049
W4m0m2	22.5	132	98.48	0.77	-0.001 ± 0.048
W4p1m0	22.5	395	92.91	0.82	0.006 ± 0.045
W4p1m1	22.5	908	95.70	1.96	-0.010 ± 0.051
W4p1m2	22.5	416	95.19	1.26	0.001 ± 0.051
W4p2m0	22.5	274	94.89	0.77	-0.013 ± 0.045
W4p2m1	22.5	517	96.52	1.00	-0.006 ± 0.051
W4p2m2	22.5	263	94.30	0.40	-0.007 ± 0.050

^a The number of uniquely matched sources between our catalogues and high-confidence VVDS objects (see also text); ^b the percentage of sources from column three (N) with a high-confidence BPZ photo- z estimate ($\text{ODDS} > 0.9$); ^c defined as the percentage of galaxies with $(z_{\text{phot}} - z_{\text{spec}})/(1 + z_{\text{spec}}) > 0.15$; ^d bias and scatter of $(z_{\text{phot}} - z_{\text{spec}})/(1 + z_{\text{spec}})$ after outlier rejection.

- we select galaxies by means of the SExtractor star-galaxy classifier CLASS_STAR and reject all sources with CLASS_STAR > 0.95;
- we include only objects with reliable photometry in all five filter bands (see above);
- finally we reject all sources with ODDS < 0.9.

Our catalogues contain in total 3.9 million galaxies outside an object mask (rejection steps 1 and 2) and finally 1.45 million sources (about 13 galaxies per sq. arcmin) with reliable BPZ photo- z estimates (object sample after all rejections).

We first compare our photo- z 's from W1 and W4 to spectroscopic redshifts from the VVDS in a similar way as presented in Hildebrandt et al. (2008). Note that these spectra were previously used to calibrate the data! Table 2 summarises the results indicating a homogeneous dispersion $\sigma_{\Delta z/(1+z)} \approx 0.04$ – 0.05 and an outlier rate (defined as the percentage of galaxies with $(z_{\text{phot}} - z_{\text{spec}})/(1 + z_{\text{spec}}) > 0.15$) of 1–2% up to $i'_{\text{AB}} = 24$. The $\sigma_{\Delta z/(1+z)}$ statistics is estimated after outliers have been rejected. If we perform the spectro- z vs. photo- z comparisons with the ODDS > 0.0 sample (but all other filters as described above) the dispersion is nearly unchanged while the outlier rate rises by a factor 3 to 8. This confirms that the ODDS parameter is a good selection criterion to reject outliers and to obtain samples of homogeneous photo- z quality up to about $i'_{\text{AB}} \approx 24$. A plot of the photo- z vs. VVDS spectro- z results in the regions W1 and W4 is shown in Fig. 4. While the figure shows an overall good performance of our photo- z estimation it reveals residual systematics. A significant tilt is present in the z_{phot} vs. z_{spec} comparison leading to a systematic overestimation of up to 0.1–0.2 of the redshift at low z_{spec} and to a underestimation at high z_{spec} . The tilt crosses the zero axis at $z = 0.5$ and hence it cancels negative and positive contributions to statistics involving Δz (see Fig. 4). The $\Delta z/(1+z)$ statistics for the complete W1 ($N = 1466$) and W4 ($N = 3488$) samples are: $\Delta z/(1+z) = -0.006 \pm 0.051$ (W1) and $\Delta z/(1+z) = -0.005 \pm 0.050$ (W4). If we split the sample

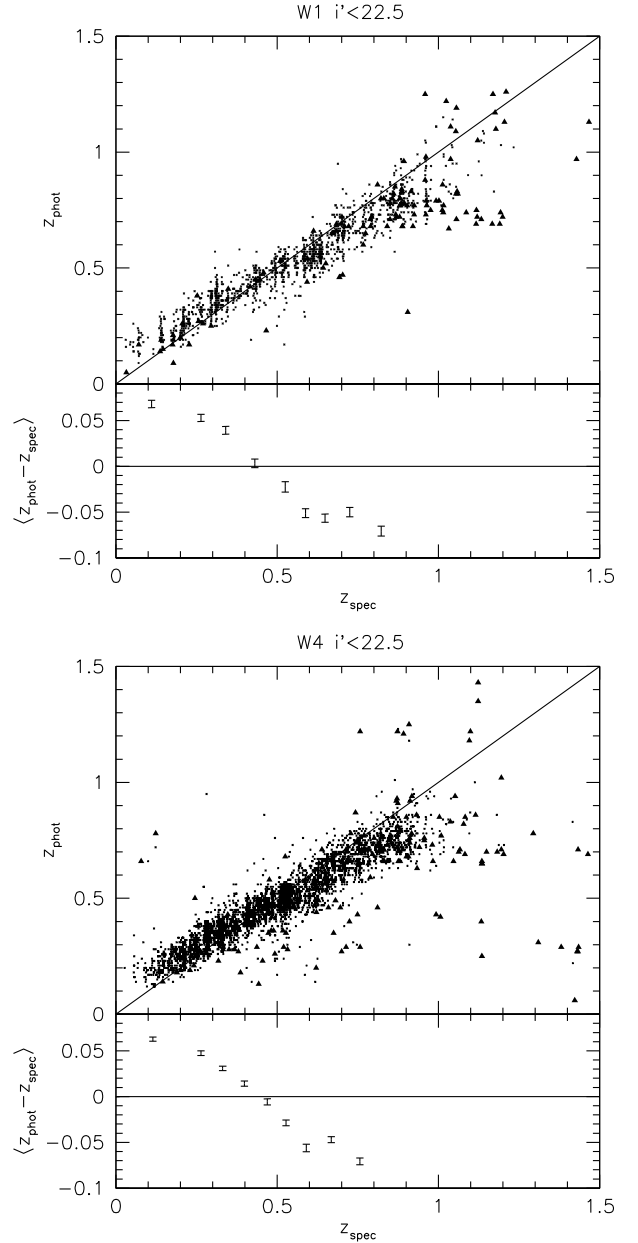


Fig. 4. Photometric vs. spectroscopic redshifts in the W1 and W4 regions: we show in the upper panels 1349 (W1) and 3312 (W4) galaxies with $i'_{\text{AB}} < 22.5$, reliable VVDS flags, good photometry in all five filter bands and ODDS > 0.9 (points). Triangles represent galaxies with $0 < \text{ODDS} < 0.9$ (117 sources in W1 and 170 objects in W4). Lower panels show a binned distribution of $\langle z_{\text{phot}} - z_{\text{spec}} \rangle$ from the ODDS > 0.9 samples of the upper panels.

at $z = 0.5$ we obtain for $z < 0.5$: $\Delta z/(1+z) = 0.03 \pm 0.043$ (W1: $N = 595$) and $\Delta z/(1+z) = 0.025 \pm 0.037$ (W4: $N = 1690$). Accordingly for $0.5 < z < 1.0$: $\Delta z/(1+z) = -0.032 \pm 0.035$ (W1: $N = 809$) and $\Delta z/(1+z) = -0.034 \pm 0.038$ (W1: $N = 1728$).

We do not try to remedy these systematics in this article but we will investigate it in a companion paper (Hildebrandt et al., in prep.). The overestimation at the low- z is mainly caused by the redshift prior in BPZ. It seems to give too little probability to the low- z population in the CARS data. A modification of the original prior in this sense removes the observed bias for $0 < z < 0.5$. The high- z underestimation of our redshifts can be corrected by a recalibration of the original Coleman et al. (1980) and Kinney et al. (1996) template sets; see also Feldmann et al. (2006). In

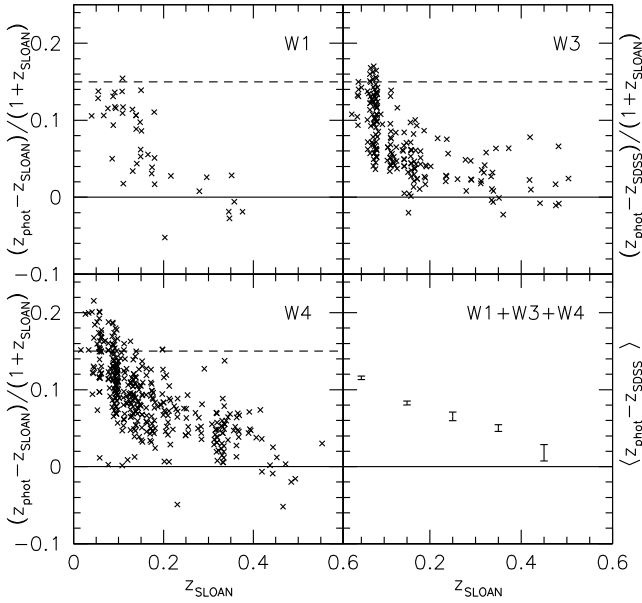


Fig. 5. Comparison of CARS BPZ photo- z against SDSS spectra ($0 < z < 0.6$): the plot shows $N = 44$ objects for W1, $N = 208$ for W3 and $N = 400$ for W4. Note the different ordinate in the lower right panel!

the following we further check the consistency and quality of our current photo- z sample.

4.1. Internal and external quality checks on our photo- z sample

Besides with the VVDS the CARS patches overlap with public spectra from the SDSS⁸ (W1–W4) and the DEEP2⁹ redshift survey (W3; Davis et al. 2007). Hence, we can test our photo- z 's which were partly calibrated and verified against the VVDS with an independent set of spectroscopic data. The comparisons are shown in Figs. 5 and 6; formal quality parameters are listed in Table 3. We observe exactly the same systematics identified in the comparisons with the VVDS spectra: a systematic tilt with overestimates of about 0.05–0.15 in the low- z regime and a reverse trend for $z > 0.5$. Our tests indicate that the photo- z quality and remaining systematics for the current CARS data set are comparable in the mean for all fields; regardless whether the galaxies profited directly from a previous calibration with spectra or whether we transferred corrections obtained with a galaxy subset to other fields. The trends we see with our BPZ photometric redshifts also show up in a comparison with previously obtained photo- z estimates with the photometric redshift code LePhare¹⁰ on the CFHTLS-Deep field D1 (see Ilbert et al. 2006). We show a direct comparison of the D1 and our W1p2p3 photometric redshift estimates in Fig. 7. The figure confirms an overall very good agreement and a systematic tilt for $0 < z < 1$ in our estimates; our high-confidence BPZ photo- z sample with $i'_{AB} \leq 24$ has 24558 common objects with the Ilbert et al. (2006) catalogue. The latter was filtered for $(z_{up1\sigma} - z_{inf1\sigma}) / (1 + z_{Ilbert}) < 0.25$. For the complete common sample with $i'_{AB} \leq 24$ we measure $\Delta z = (z_{phot} - z_{Ilbert}) = -0.02 \pm 0.11$.

⁸ Spectroscopic data were obtained from <http://cas.sdss.org/astro/en/tools/search/SQS.asp>

⁹ Spectroscopic data were obtained from <http://deep.berkeley.edu/DR3>

¹⁰ See http://www.oamp.fr/people/arnouts/LE_PHARE.html

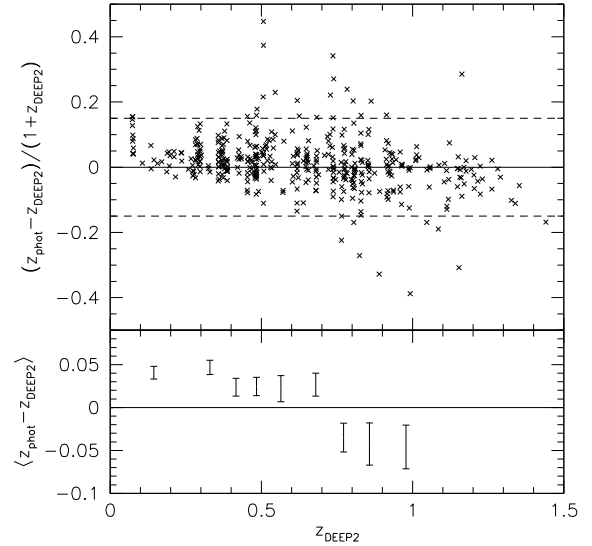


Fig. 6. Comparison of CARS BPZ photo- z against DEEP2 spectra for $0 < z < 1.5$: shown are $N = 448$ common objects between the DEEP2 redshift survey and the CARS fields W3m1m2 and W3m1m3.

Table 3. Quality parameters for the comparison of CARS BPZ photo- z against SDSS and DEEP2 spectra.

Field	Survey	z -coverage ^a	N	η [%]	$\Delta z / (1 + z)$
W1	SDSS	$0 < z < 0.6$	44	2.4	0.069 ± 0.050
W3	SDSS	$0 < z < 0.6$	208	4.8	0.068 ± 0.042
W4	SDSS	$0 < z < 0.6$	400	12.8	0.080 ± 0.039
W3	DEEP2	$0 < z < 1.5$	448	7.3	0.010 ± 0.050

^a Redshift range probed by the spectroscopic sample.

Finally we perform two internal consistency checks on our estimates. The first one is a comparison of independent estimates from overlap objects in different CARS pointings (see Fig. 1). In Fig. 8 we show on a patch basis $\Delta z_{phot} = (z_{phot1} - z_{phot2})$ for all overlap sources. The means and scatters of this quantity for individual patches are: $\Delta z_{phot} = 0.0002 \pm 0.0772$ (W1; 24 329 objects), $\Delta z_{phot} = -0.00005 \pm 0.0767$ (W3; 6211 objects) and $\Delta z_{phot} = -0.0006 \pm 0.0723$ (W4; 16 849 objects). The plot and the numbers demonstrate a homogeneous and robust redshift estimation over the whole CARS area. Note that this comparison includes areas with and without spectroscopic calibration overlap. The second internal consistency check are the redshift distributions for the three CARS patches. Figure 9 shows that they are very comparable for all three CARS patches.

4.1.1. Angular cross-correlation of galaxy populations in different photo- z redshift bins

In the following we apply a correlation function analysis to further quantify the reliability and suitability of photometric redshift estimates. The theoretical background will be detailed in Benjamin et al. (in prep.). Judging photo- z quality by calibration with external spectroscopy provides us with an overall picture of the dispersion of our estimates and the total rate of *catastrophic outliers*. First, this quality control is limited to the magnitude and/or redshift range of our external comparison sample and second we often need a more detailed picture on the photo- z (re)distribution of galaxies in redshift space. For instance, weak lensing tomography studies of the cosmic shear effect do not require a precise redshift estimate for each individual galaxy.

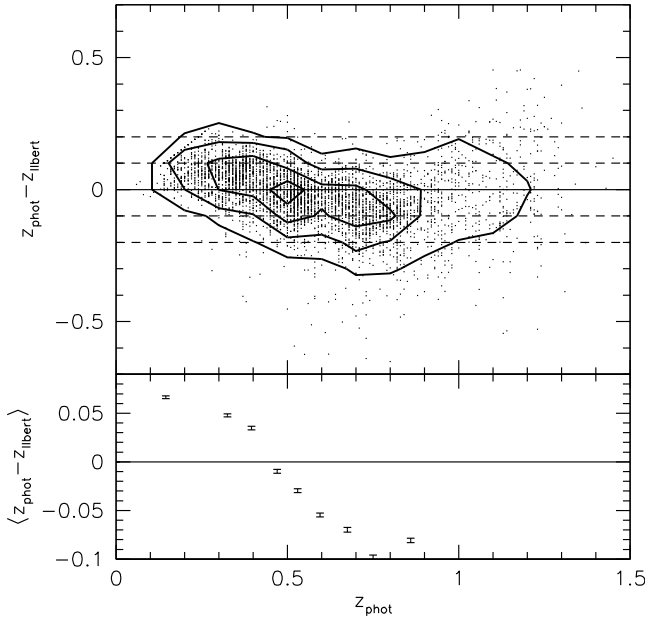


Fig. 7. Comparison of our BPZ photo- z estimates on W1p2p3 with those from Ilbert et al. (2006) on the CFHTLS-Deep D1 field. The comparison includes 24 558 common objects with a pre-filtering for high-confidence sources in both catalogues and $i'_{AB} \leq 24$ (see text for details). 853 objects (3.89%) lie outside the plotting region of $-0.7 < z_{\text{phot}} - z_{\text{Ilbert}} < 0.7$. We show one point out of five for clarity of the plot; contours indicate areas of 0.8, 0.5, 0.25 and 0.05 times the peak-value of the point-density distribution.

However, we need to reliably separate galaxies into redshift bins and we require a precise understanding of our errors concerning redshift misidentifications and inter-bin contamination factors (see e.g. Huterer et al. 2006).

To quantify the crucial error contribution due to large systematic redshift misidentifications we investigate the angular cross-correlation function of galaxies in different photo- z slices. The cross-correlation technique has already been advocated as a way to reconstruct the source redshift distribution (Schneider et al. 2006), or, in combination with spectroscopic redshift, as a way to improve the photo- z calibration (see Mandelbaum et al. 2008).

For accurate redshift estimates we expect to see a strong auto-correlation in individual redshift bins and, due to the expected photo- z scattering ($\sigma_{\Delta z} \approx 0.05-0.1$), a lower-level cross-correlation signal in neighbouring slices. But one would not expect to see a cross-correlation signal for slices that are physically far apart. Contamination by catastrophic photo- z failures would lead to significant amplitudes of the angular cross-correlation function of photo- z slices that are well separated in redshift. In Fig. 10 we show a correlation slice-analysis of the CARS photo- z estimates for objects with $i'_{AB} < 24$. It represents a matrix plot including the angular cross-correlation functions of all pairs of photo- z slices. The figure illustrates the expected behaviour: we observe a very significant autocorrelation and a decreasing cross-correlation in neighbouring bins. Our analysis also shows a decent signal for the highest redshift bins ($z \geq 1.5$) with low- z slices. This shows that high- z tails, which are often observed in redshift distributions derived from photo- z 's, are populated with true low- z galaxies. We note that the ODDS > 0.9 filtering applied hitherto rejects large parts of dubious sources with a very broad or doubly peaked photometric redshift probability distribution. To visualise the effect of low- z high- z contamination we

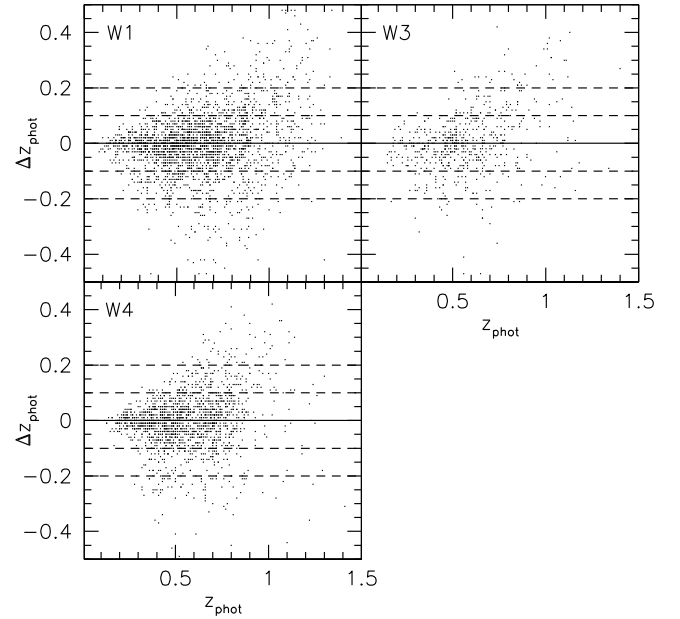


Fig. 8. Consistency of our photometric redshift estimates: we compare independent photo- z measurements from objects appearing in multiple CARS pointings in each patch (W1: $N = 24\,329$; W3: $N = 6\,211$; W4: $N = 16\,849$). Dashed lines mark regions with $\Delta z_{\text{phot}} = 0.1, 0.2$. Only 1 out of 10 points is shown for clarity of the plots. See the text for further details.

relaxed our filtering to ODDS > 0.8 in the cross-correlation analysis.

In Fig. 10 we show separately the correlation functions of the faintest objects with $23 < i'_{AB} < 24$. We see that the faint population of our galaxies behaves exactly in the same way as the complete sample. This indicates that the photo- z accuracy does not degrade in the lower S/N regime.

While Fig. 10 already allows us to draw important qualitative conclusions we can derive formulae for the mutual contamination of redshift bins. A complete matrix description of the formalism, which will allow a consistent analysis of the results in Fig. 10, will be presented elsewhere (Benjamin et al., in prep.). In this paper we limit the discussion to a strict pairwise cross-correlation analysis, i.e. we present quantitative results only for cases where the whole redshift sample is split in exactly two bins.

The basic idea is to infer the degree of contamination between two redshift slices from the measurement of the cross-correlation w_{12} between the bins.

The fraction of galaxies from bin 1 present in bin 2, as a fraction of the true number of galaxies in bin 1 (N_1^T), is f_{12} . Likewise the fraction of galaxies in bin 1 from bin 2 is given by f_{21} , which is defined such that the number of galaxies present in bin 1 from bin 2 is given by $N_2^T f_{21}$. Hence the observed number of galaxies in each bin (N^o) can be expressed as,

$$N_1^o = N_1^T(1 - f_{12}) + N_2^T f_{21},$$

$$N_2^o = N_2^T(1 - f_{21}) + N_1^T f_{12}. \quad (4)$$

The first term of each equation accounts for those galaxies that do not leave the given bin, the second term accounts for those interloping galaxies from the other bin. Inverting these equations,

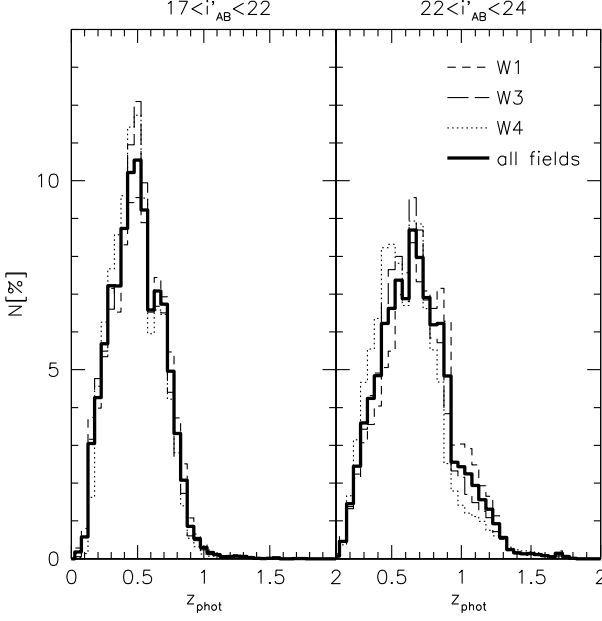


Fig. 9. Normalised distributions of our high-confidence photometric redshift estimates for all CARS patches (W1: $N = 205\,956$ for $17 < i'_{AB} < 22$ and $N = 487\,593$ for $22 < i'_{AB} < 24$; W3: $N = 52\,295$ for $17 < i'_{AB} < 22$ and $N = 119\,589$ for $22 < i'_{AB} < 24$; W4: $N = 104\,417$ for $17 < i'_{AB} < 22$ and $N = 252\,969$ for $22 < i'_{AB} < 24$); all distributions have only very few objects beyond redshift 2 (not shown).

the true number of galaxies can be expressed as a function of the observed numbers and the fractions f_{12} and f_{21} ,

$$\begin{aligned} N_1^T &= \frac{N_1^o - f_{21}(N_1^o + N_2^o)}{1 - f_{12} - f_{21}}, \\ N_2^T &= \frac{N_2^o - f_{12}(N_1^o + N_2^o)}{1 - f_{12} - f_{21}}. \end{aligned} \quad (5)$$

Note that $N_1^o + N_2^o = N_1^T + N_2^T$, thus the total number of galaxies is preserved, as should be the case. It is also obvious that for cases where $f_{12} + f_{21}$ is unity there is a zero in the denominator. What is less clear, is that in these cases the numerator is also zero, which can be seen by plugging Eq. (4) into the numerator. In this case the system of equations is degenerate, and will not admit a unique solution. This should not pose a practical limitation since it is expected that the fractional contamination between bins is small, and specifically less than 0.5.

In order to calculate how the cross-correlation function is changed for non-vanishing coefficients f_{12} , f_{21} , it is sufficient to consider the natural estimator of the angular correlation function, as opposed to that presented by Landy & Szalay (1993). The natural estimator works well at small and intermediate scales where edge effects are not an issue, provided that there is a sufficient density of points (see Kerscher et al. 2000, for a comparison of the estimators). The observed angular cross correlation functions are given by,

$$1 + \omega_{11}^o = \frac{(D_1 D_1)_\theta^o}{(R_1 R_2)_\theta}, \quad (6)$$

$$1 + \omega_{12}^o = \frac{(D_1 D_2)_\theta^o}{(R_1 R_2)_\theta}, \quad (7)$$

where $(D_1 D_1)_\theta^o$ is the observed number of pairs separated by angle θ within bin 1, similarly $(D_1 D_2)_\theta^o$ is the number of pairs between bins 1 and 2, and $(R_1 R_2)_\theta$ is the number of pairs between objects from random fields of identical geometry.

Considering how galaxy pairs are split between the two bins 1 and 2, one can show that the observed number of pairs depends on a combination of the true number of pairs and the contamination fractions:

$$\begin{aligned} (D_1 D_2)_\theta^o &= (D_1 D_2)_\theta^T ((1 - f_{12})(1 - f_{21}) + f_{21} f_{12}) \\ &\quad + (D_1 D_1)_\theta^T (1 - f_{12}) f_{21} + (D_2 D_2)_\theta^T f_{21} (1 - f_{21}). \end{aligned} \quad (8)$$

Plugging this relation into Eq. (7), and noting that the term $(D_1 D_2)_\theta^o / (R_1 R_2)_\theta$ must be normalised by $N_1^R N_2^R / N_1^o N_2^o$, where $N_{1,2}^R$ is the number of objects in the random samples, the following equation can be derived for the observed angular cross-correlation function,

$$\begin{aligned} 1 + \omega_{12}^o &= (1 + \omega_{11}^T) \frac{(N_1^T)^2}{N_1^o N_2^o} f_{12} (1 - f_{12}) \\ &\quad + (1 + \omega_{22}^T) \frac{(N_2^T)^2}{N_1^o N_2^o} f_{21} (1 - f_{21}) \\ &\quad + (1 + \omega_{12}^T) \frac{N_1^T N_2^T}{N_1^o N_2^o} (1 - f_{12} - f_{21} + 2f_{12} f_{21}). \end{aligned} \quad (9)$$

Note that the observed cross-correlation function depends on the unknown true number of galaxies in the bins and the unknown true auto-correlation function. The true galaxy number can be expressed in terms of the observed number of galaxies and the contamination fractions via Eq. (5). It is possible to express the true auto-correlation as functions of contamination fractions, the number of observed galaxies and the observed auto-correlation functions (Benjamin et al., in prep.),

$$\begin{aligned} \omega_{11}^T &= \omega_{11}^o \left(\frac{N_1^o}{N_1^T} \right)^2 \frac{(1 - f_{21})^2}{(1 - f_{12})^2 (1 - f_{21})^2 - f_{12}^2 f_{21}^2} \\ &\quad - \omega_{22}^o \left(\frac{N_2^o}{N_1^T} \right)^2 \frac{f_{21}^2}{(1 - f_{12})^2 (1 - f_{21})^2 - f_{12}^2 f_{21}^2} \\ &\quad - \omega_{12}^T \left(\frac{N_2^T}{N_1^T} \right) \frac{2f_{21} (1 - f_{21})}{(1 - f_{12})(1 - f_{21}) + f_{12} f_{21}}. \end{aligned} \quad (10)$$

By exchanging 1 and 2 in Eq. (10) an equivalent expression for the auto-correlation of bin 2 is obtained. To finally use Eqs. (9) and (10) we make the explicit assumption that the true cross-correlation between the two redshift bins is zero ($\omega_{12}^T = 0$), i.e. all the observed cross-correlation is due to contamination. This prescription allows us to use the observed correlation functions and number of galaxies to determine the contamination fractions, f_{12} and f_{21} , for a pair of redshift bins.

We note that the outlined formalism cannot be trivially extended to a multi-bin setup, since it assumes a pair of bins and ignores possible contamination from other redshifts. However, it already allows us to recover the fraction of objects that cross a given redshift z_{cut} due to photometric redshift errors, and an analysis can be done as a function of z_{cut} .

We apply the pairwise analysis on our data by cutting it at $z_{\text{cut}} = 0.2; 0.3; 0.4; 0.5; 0.6; 0.7; 0.8; 0.9; 1.0; 1.5; 2.0$ yielding a low redshift bin $0.0 < z_1 < z_{\text{cut}}$ and a high redshift bin $z_{\text{cut}} < z_2 < 4.0$. The angular auto and cross-correlation functions from the pair of bins are used to estimate the contamination fractions f_{12} and f_{21} by fitting the observed cross-correlation with Eq. (9). The analysis was performed with eleven equally spaced cross-correlation bins ranging from 0.9 to 10.0. We checked with an analysis of three and five bins that our results do not depend significantly on this choice. This step is followed by a minimum chi-square analysis and the likelihood contours in the contamination fraction parameter space are presented in Fig. 11. The

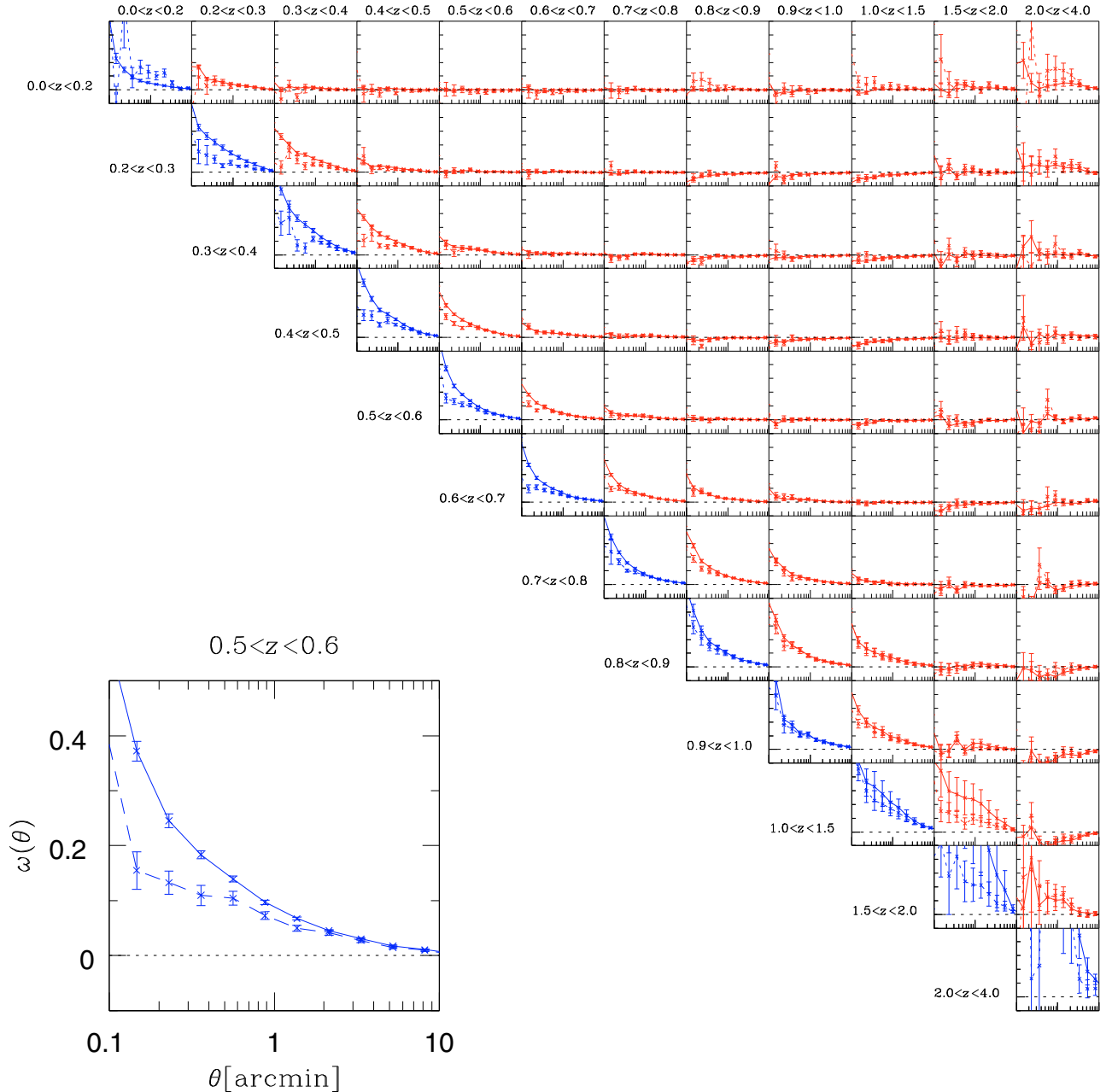


Fig. 10. The angular cross-correlation of objects in different photo- z slices (*solid* lines represent objects with $i'_{AB} < 24$ and *dashed* lines represent objects with $23 < i'_{AB} < 24$): the matrix plot represents the complete CARS area and each panel shows the qualitative behaviour of auto- (diagonal) and crosscorrelation (off-diagonal) measurement for different redshift slices. The rows represent bins from $z = 0$ to $z = 3.9$ (steps $z = 0.0; 0.2; 0.3; 0.4; 0.5; 0.6; 0.7; 0.8; 0.9; 1.0; 1.5; 2.0; 3.9$). *The lower left panel* is a zoom-in to the corresponding panel of the matrix plot. Note that in the cross-correlation analysis we include all objects with $ODDS > 0.8$. See text for further details.

degeneracy between the two contamination fractions is clearly evident, and lower and upper limits can be estimated.

For the lowest redshift cuts there is a strong degeneracy, with $0.0 < f_{12} < 0.6$, and $f_{21} \sim 0.01$, hence a potentially large fraction of low redshift galaxies are expected to be at higher redshift. Likewise for the highest redshift cuts a potentially large fraction of high redshift galaxies are expected to be at lower redshifts. It is important to reiterate that the fraction f_{12} is the number of galaxies that move from bin 1 to bin 2 as a fraction of the true number of galaxies in bin 1. Hence, the observed large degeneracies in the low and high redshift cuts are a consequence of the very different occupation numbers in the two bins. For the

intermediate redshift cut range $0.4 < z_{cut} < 0.9$ the contamination factors are around 10–20%.

The spectroscopic data in W1 allow us to directly calculate contamination fractions f_{12} and f_{21} for the field W1p2p3 and to check whether our estimates obtained via correlation functions are reasonable. The VVDS in this field has the same depth as the limiting magnitude of our correlation analysis sample ($i'_{AB} \leq 24.0$). We subdivide galaxies according to spectroscopic (true) redshifts and determine directly contamination fractions with the photometric redshifts. Error contributions on this quantity are the Poisson noise and the redshift sample variance in a field of 1 sq. degree. The latter was estimated in

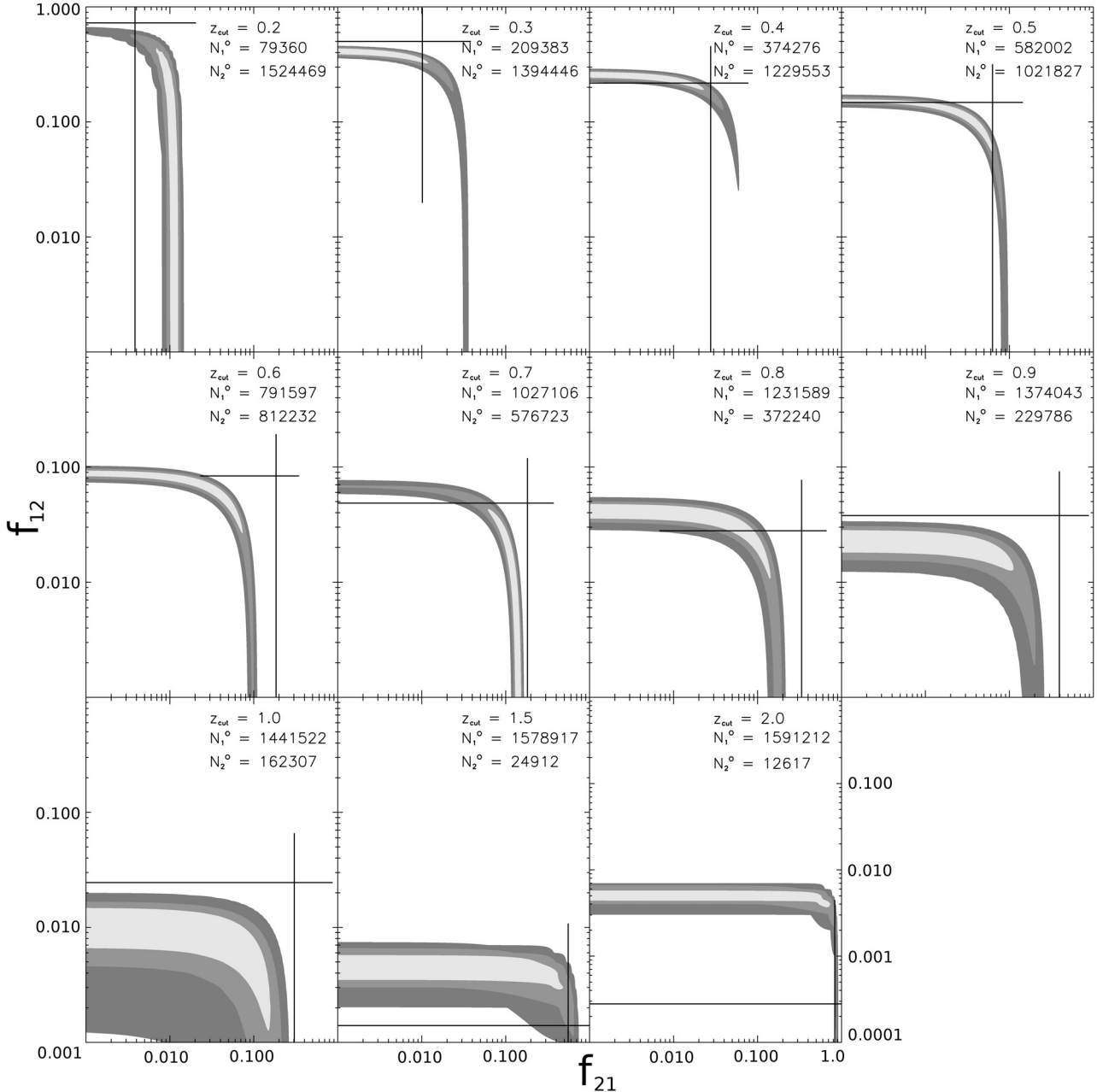


Fig. 11. The estimated contamination fractions, f_{12} and f_{21} resulting from a strict pairwise cross-correlation analysis. The two redshift bins are defined to be $0.0 < z_1 < z_{\text{cut}}$ and $z_{\text{cut}} < z_2 < 4.0$. Contours indicate the 1, 2 and 3-sigma confidence regions, having progressively darker shades of grey. Legends in the figure give the observed number of galaxies in each bin. The data points with error bars denote the measured contamination fraction found for those galaxies in the VVDS W1 spectroscopic sample (see text for details). Note that for $z_{\text{cut}} = 1.5$ and $z_{\text{cut}} = 2.0$ an extended vertical scale is used in order to show the measured contamination.

van Waerbeke et al. (2006) to be 15 times the Poisson contribution. We plot our results in Fig. 11. We see that the contamination fractions determined with spectroscopic redshifts in one field are very comparable to the correlation function estimates for the whole CARS surveys. This directly shows the validity of our analysis.

5. Available data products

We make available on request our multi-colour catalogues including photo- z estimates of 37 CARS fields (corresponding to $\sim 30 \text{ deg}^2$ effective survey area after image masking). The data package includes object catalogues, the derived image masks and JPEG images to inspect colour data and extracted sources.

The catalogues are available as FITS binary tables and a subset of the most important entries as UNIX-ASCII text files.

The FITS catalogue version includes most of the original SExtractor keywords and for their meaning we refer to the SExtractor manual (Bertin 2003). All these basic keys are measured in a SExtractor run in dual-image mode where we use the unconvolved i -band image for detection as well as for photometric measurements (see Sect. 3.3).

Additional keywords created in subsequent SExtractor runs with the PSF-matched images in the five bands for photometric colour measurements are indicated by an additional $_x$ where $x \in [u^*, g', r', i', z']$. In particular, these are the different kinds of fluxes, magnitudes and corresponding error

Table 4. Description of the most important FITS keys in the CARS multi-colour catalogues.

key name	Description	Unit	Measured on	ASCII catalogue
SeqNr	Running object number	–	–	✓
ALPHA_J2000	Right ascension	degree	unconvolved i' -band image	✓
DELTA_J2000	Declination	degree	unconvolved i' -band image	✓
Xpos	x pixel position	pixel	unconvolved i' -band image	✓
Ypos	y pixel position	pixel	unconvolved i' -band image	✓
MAG_AUTO	total i' -band magnitude	mag	unconvolved i' -band image	✓
MAGERR_AUTO	total i' -band magnitude error	mag	unconvolved i' -band image	✓
MAG_ISO_x ^a	isophotal magnitude in x -band	mag	PSF-equalised x -band image	✓
MAGERR_ISO_x	isophotal magnitude error in x -band	mag	PSF-equalised x -band image	✓
MAG_APER_x ^b	aperture magnitude vector in x -band	mag	PSF-equalised x -band image	✓
MAGERR_APER_x	aperture magnitude error vector in x -band	mag	PSF-equalised x -band image	✓
FWHM_WORLD	FWHM assuming a Gaussian core	degree	unconvolved i' -band image	✓
FLUX_RADIUS	half-light-radius	pixel	unconvolved i' -band image	✓
A_WORLD	profile rms along major axis	degree	unconvolved i' -band image	✓
B_WORLD	profile rms along minor axis	degree	unconvolved i' -band image	✓
THETA_J2000	position angle	degree	unconvolved i' -band image	✓
CLASS_STAR	star-galaxy classifier	–	unconvolved i' -band image	✓
Flag	SExtractor extraction flags	–	unconvolved i' -band image	✓
FLUX_ISO_x	isophotal flux in x -band	ADU/s	PSF-equalised x -band image	–
FLUXERR_ISO_x	isophotal flux error in x -band	ADU/s	PSF-equalised x -band image	–
FLUX_APER_x	aperture flux vector in x -band	ADU/s	PSF-equalised x -band image	–
FLUXERR_APER_x	aperture flux error vector in x -band	ADU/s	PSF-equalised x -band image	–
MAG_LIM_x	limiting magnitude in x -band	mag	unconvolved x -band image	✓
Z_B	Bayesian photo- z estimate	–	–	✓
Z_B_MIN	lower bound of the 95% confidence interval	–	–	–
Z_B_MAX	upper bound of the 95% confidence interval	–	–	–
T_B	best-fit spectral type ^c	–	–	✓
ODDS	empirical odds ^d	–	–	✓
NBPZ_GOODFILT	filters with reliable photometry	–	–	✓
NBPZ_BADFILT	filters with $MAGERR_ISO \geq 1.0$	–	✓	–
NBPZ_LIMFILT	filters with $MAG_ISO_x \geq MAG_LIM_x$	–	–	✓
MASK	global mask key ^e	–	–	✓

^a $x \in [u, g, r, i, z]$; ^b The ASCII catalogue version contains one aperture magnitude at a diameter of $1''.86$. The FITS version lists 24 aperture magnitudes for diameters from $0''.744$ to $10''.23$; ^c E11 = 1, Sbc = 2, Scd = 3, Im = 4, SB3 = 5, SB2 = 6, plus two interpolated types in colour-redshift space between each pair of these basis templates. Intermediate best-fit templates are indicated by a floating point number for T_B; ^d integrated probability inside an interval which is such that it contains 95% probability for a single Gaussian; ^e unification of the different masks described in Sect. 3.4.

estimates (e.g. FLUX_AUTO_x, FLUXERR_AUTO_x, MAG_ISO_x, MAGERR_ISO_x, etc.); note that magnitude error estimates in the catalogues do not take into account systematic zeropoint offsets but only statistical errors due to photon noise. We estimate 24 different aperture fluxes and magnitudes with diameters ranging from 4 to 55 pixels ($\approx 0''.744$ to $10''.23$). We add the 1σ limiting magnitudes MAG_LIM_x as described in Sect. 3.2. All magnitudes are provided in MegaPrime instrumental AB magnitudes. We note that we did not apply any magnitude correction to the catalogue entries also if our tests performed in Sect. A.4 might justify them. This especially applies for discrepancies present in the u^* -band calibration of the W3 and W4 pointings (see Sect. A.4). To allow an easy identification of objects with problematic photometry we add the flags NBPZ_GOODFILT indicating the number of filters with reliable photometry, NBPZ_BADFILT giving the number of filters with $MAGERR_ISO_x \geq 1.0$ and NBPZ_LIMFILT listing the number of filters with MAG_ISO_x fainter than our formal magnitude limit (see Sect. 2). Which of these three properties applies to which filters is encoded in additional keys.

Furthermore, we provide a global mask key MASK which is 0 for objects that do not lie inside one of our object masks and 1 otherwise. This key takes into account all masks from our object density, bright star and asteroid track analyses as described in Sect. 3.4.

Finally, the catalogues contain photo- z relevant quantities from the output of BPZ. Besides the Bayesian redshift estimate, Z_B, we include the ODDS probability, the SED corresponding to the Bayesian redshift (T_B), the corresponding χ^2 , the 95% confidence interval (Z_B_MIN and Z_B_MAX) as well as the maximum-likelihood redshift and type estimate (Z_ML and T_ML), which are put out by BPZ before the prior is applied.

The most important catalogue entries are summarised in Table 4.

6. Summary and conclusions

We have presented high-quality five-band multi-colour data from 37 sq. deg. of the CARS survey. We gave a detailed description of our data-handling procedures ranging from data selection to the final catalogues including a first set of photometric redshift estimates. Our algorithms provide an accurate astrometric alignment on the sub-pixel level to extract precise object colour information. For the large majority of our data the Elixir photometric information allows us to derive an unbiased absolute photometric calibration with a scatter of $\sigma \approx 0.02$ – 0.05 mag on a pointing basis for $g'r'i'z'$; tests against the official TERAPIX T0003 CFHTLS-data release show very significant zeropoint offsets for four out of 93 common fields. In u^* direct

comparisons with SDSS suggest that our zeropoints are systematically about 0.1 mag too faint.

We showed that our colour catalogues allow, with the help of spectroscopic information, the estimation of reliable photometric redshift estimates with the method of Benitez (2000). In our 37 sq. deg. survey (about 30 sq. deg. in unmasked areas) we detect about 3.9 million objects classified as galaxies (SEXTRACTOR CLASS_STAR < 0.95). From those about 1.45 million (10–15 galaxies per sq. arcmin) have a formally reliable photo- z estimate with ODDS > 0.9 (completeness 37.2%). Comparing our photo- z estimates with external spectroscopic data we find an overall performance of $\sigma(\Delta z/(1+z)) \approx 0.04-0.05$ up to $i'_{AB} \approx 24$ with an outlier rate of $\eta \approx 1-3\%$. We applied a cross-correlation analysis to qualitatively investigate redshift slice contamination between samples in different redshift bins. It indicates significant contamination of neighbouring redshift slices with a width of $\Delta z \approx 0.1$ and a dying correlation signal for bins more than $\Delta z \approx 0.3$ apart. Catastrophic outliers occur between low- z bins and galaxies with an estimate of $z_{\text{phot}} \geq 1.5$. We performed a more quantitative analysis only for the case when our whole redshift sample is divided in exactly two redshift bins. With the help of spectroscopic redshifts from the deep part of the VVDS it reconfirms the homogeneity of our photo- z sample over the entire CARS area. A more complete, in-depth analysis with the correlation function technique will be presented in Benjamin et al. (in prep.).

We note that the catalogues and the estimation of photo- z 's was optimised for studies in the regime $0 < z < 1.4$ and objects with a larger estimate should be filtered. The current catalogues are not suited for studies of the high- z regime such as u^* -band drop-out searches. While the photo- z performance according to formal parameters is very good our estimates show a systematic tilt for $0 < z < 1$ (higher redshift ranges cannot be verified due to the lack of spectroscopic information). Our estimates are too high by $\Delta z \approx 0.1$ for low z and the bias decreases linearly to reach about $\Delta z \approx -0.1$ for $z \approx 1$. The zero-crossing of the tilt is at $z \approx 0.5$. The mean bias is about $\langle \Delta z \rangle \approx 0.03$ for $z < 0.5$ and about $\langle \Delta z \rangle \approx -0.03$ for $0.5 < z < 1$. Improved and bias-free BPZ photo- z estimates will be presented in Hildebrandt et al. (in preparation). Additionally, photo- z estimates with the method of Bender et al. (2001) are analysed and compared to our current work in Brimiouille et al. (2008). An independent effort to derive photo- z estimates on the same survey area with the TERAPIX T0004 release is undertaken in Coupon et al. (2008).

The presented catalogues mark the first step for the primary science goal of CARS in the CFHTLS-Wide area: the assembling of a galaxy cluster sample from low to high redshift and its subsequent exploitation for cosmological studies. For the second step in this effort, our multi-colour data are currently being used on several cluster detection algorithms: the Voronoi tessellation technique from Ramella et al. (2001), the Postman matched filter algorithm (see Postman et al. 1996) and the Red-Cluster Sequence technique (see Gladders & Yee 2000).

To trigger a larger variety of follow-up studies we make available our catalogues on request.

Acknowledgements. We thank Brice Ménard for help with the redshift cross-correlation analysis and Stephen Gwyn for clarifications on his MegaPipe processing pipeline. We thank the staff at the Canada-France-Hawaii Telescope and at the TERAPIX data centre in Paris for delivering high-quality CFHTLS Survey products and excellent image processing software to the astronomical community. The anonymous referee helped us to improve the manuscript significantly. We acknowledge use of the Canadian Astronomy Data Centre, which is operated by the Dominion Astrophysical Observatory for the National Research Council of Canada's Herzberg Institute of Astrophysics. This work was supported by the DFG Sonderforschungsbereich 375 "Astro-Teilchenphysik", the DFG

priority program SPP-1177 "Witnesses of Cosmic History: Formation and evolution of black holes, galaxies and their environment" (project IDs ER327/2-2, SCHN 342/7-1, Se1038/1), the German Ministry for Science and Education (BMBF) through DESY under the project 05AV5PDA/3 and the TR33 "The Dark Universe". H. H. and M. L. are supported by the European DUEL RTN, project MRTN-CT-2006-036133. T.S. acknowledges financial support from the Netherlands Organization for Scientific Research (NWO). K.H. is supported by the Research council of Norway, project number 177254/V30. L.v.W. and J.B. acknowledge support by NSERC and Cifar. Part of the data reduction described in this work was performed on CFI funded equipment under project grant #10052. M.L. thanks the University of Bonn and the University of British Columbia for hospitality.

Appendix A: Details on the data handling of CARS observations

In this Appendix we give a more detailed description on our data handling procedures of the CARS survey. The excellent Elixir preprocessing of the CARS data and the available meta-data information (see below) allowed us to build up a complete survey pipeline starting from data retrieval up to final co-added science images. The construction of our data-processing pipeline and many choices for our data-handling as described below were driven by the following two requirements:

1. The system allows a 100% automatic processing of the data with the need for manual intervention only at the final verification stage of co-added science images. This particularly forbids manual passes through all individual Elixir images either to visually grade data or to remove/mask artefacts. We needed to automatically reject problematic exposures or parts of them from the whole analysis or we need to deal with remaining defects at the level of the final science images. For instance, our automatic satellite track removal module reliably detects and removes about 95% of all bright satellite trails. If necessary, the remaining 5% need to be masked manually in the final science images.
2. We want to independently and incrementally process individual pointings as soon as the full five band coverage of a particular area is becoming publicly available.

We completely achieved the first goal and the complete data processing of the CARS data is done by one of the authors with two computers (a double processor Athlon2800+ with 4 GB Virtual memory and a quad processor/dual core AMD Opteron 885 with 11 GB of RAM) and a total disk storage capacity of about 10 Terabytes. The second goal could not be met for the photometric calibration of several fields and we needed to use information from adjacent pointings to obtain an absolute flux calibration (see below).

Most of our algorithms to process optical data from multi-chip cameras were described in Erben et al. (2005) and Hildebrandt et al. (2006) in the context of GaBoDS data (see e. g. Schirmer et al. 2003) from the 8-chip instrument WFI@MPG/ESO2.2m. We therefore limit the discussion to peculiarities of the CARS data, necessary pipeline upgrades due to the four times larger field-of-view of MegaPrime and quality assessments of our final science images.

A.1. Data preselection and retrieval

As described in Sect. 2, the starting point of the current CARS data set are the Elixir preprocessed images from the CFHTLS-Wide Survey. Besides the images, comprehensive information on the current status of the Survey and the observed data is available in the form of a CFHTLS

exposure catalogue (see <http://www.cfht.hawaii.edu/Science/CFHTLS-DATA/exposurescatalogs.html>). From the CFHTLS-Wide we preselect all pointings which are publicly available at 18/01/2008 and which have observations in the complete $u^*g'r'i'z'$ filter set.

For each survey-image a Service Observer quality flag ranging from 1–5 is available. A “1” states that the exposure was obtained within survey specifications and has no obvious defects. A “2” means that one of the predefined specifications for that exposure (seeing, sky transparency or moon phase) was out of bounds. A flag of three or higher indicates poor observing conditions or other severe defects such as tracking problems during the exposure. Only images with flags “1” or “2” enter our processing. We visually inspected in total 300 Elixir preprocessed MegaPrime exposures (60 in each filter) to verify the suitability of this quality assessment for a blind and automatic preselection of CARS data. On the other hand we did not check whether a subset of the images with higher flags still could be included in our survey.

We use the aforementioned information and the possibility to request CADC files and data products directly within programs or shell scripts¹¹ to automatically retrieve the images of interest. For the current work we transferred in total 1246 MegaPrime CFHTLS-Wide images from CADC.

A.2. Data preprocessing and weight image creation

The Elixir preprocessing includes all necessary operations to remove the instrumental signature from raw data. The data on which we start our analysis are bias-corrected and flat-fielded. Moreover, fringes are removed in i' and z' observations, permanent bad CCD pixels are marked and all images are corrected for photometric non-uniformities across the MegaPrime field-of-view; see the www pages <http://www.cfht.hawaii.edu/Science/CFHTLS-DATA/dataprocessing.html> and <http://www.cfht.hawaii.edu/Science/CFHTLS-DATA/megaprimecalibration.html> for a more detailed description of the Elixir processing.

The visual appearance of the Elixir processed data is very good. Only fringe residuals are observed for parts of the z' data. As discussed within Fig. 2 individual chips of certain exposures might not contain useful data. The first step of our own processing is therefore to identify problematic chips by considering pixel statistics and to mark them as unusable. More precisely, we exclude chips with the following defects from any further analysis: (1) the pixel value at the lower quartile of the chip pixelvalue-distribution is 10 or lower. This means that large fractions of the chip contain zeros; (2) more than 3% of the pixels in a chip are saturated. This means that a considerable chip-area is *contaminated* by a very bright star which would most probably lead to problems in the later astrometric calibration. Furthermore, at the level of science analysis such areas would be excluded anyway; (3) to astrometrically calibrate our data we first tie the i' observations to the USNO-B1 catalogue and then extract from the stacked i' image a deeper astrometric reference system for the other colours. This is discussed in more detail in Sect. A.3 below. For this reason we exclude from $u^*g'r'i'z'$ all chips which have been identified as bad in the corresponding i' -band data. In the following we updated all our THELI pipeline modules to smoothly handle an arbitrary geometry of usable chips within a CCD-array.

¹¹ See <http://www1.cadc-ccda.hia-ihp.nrc-cnrc.gc.ca/getData/doc>

To prepare the extraction of object catalogues for astrometric calibration we create for each chip a corresponding weight map which contains information on bad pixels and the relative noise properties of the image pixels. The steps of our weight image creation are described in detail in Sect. 6 of Erben et al. (2005). For the CARS data we updated and expanded our procedures as follows:

1. For the WFI@MPG/ESO2.2m camera, the starting point of our weight maps was a normalised flat-field image. A flat-field maps the relative sensitivity of image pixels within a CCD array and allows us to take into account associated pixel noise variations during object extraction. For the CARS data we neglect this effect and start the weight creation with a flat image with a pixel value of “1” on the whole array. We verified that this simplification has no significant effect on our object catalogues of single frames and of the final co-added science images later-on. It allows us to store weight images very efficiently and with significantly reduced hard-disk space.
2. Permanent bad pixels of the CCDs are marked in the Elixir processed science frames by a pixel value of “0”. This information is transferred to our weight maps. For WFI@MPG/ESO2.2m data defect pixels had to be identified with dark frames and/or flat-field images.
3. We used to visually identify and to mask bright satellite tracks which must be excluded from the object extraction and co-addition process. To process the CARS data we developed an automatic track detection and masking tool based on Hough transform techniques (see e.g. Duda & Hart 1972; Vandame 2001). To reliably find real tracks and to reject spurious detections due to bright stars and extended objects we use that a satellite typically contaminates several chips on the MegaPrime mosaic. When a candidate is found on a particular chip we check for detections on expected positions in other detectors. Tracks which are found in two or more chips are masked on all CCDs crossing their path including an additional margin of one CCD on both sides of the track. In this way also detectors on which a track cannot be detected individually are appropriately covered by an image mask. From manual inspection of 60 MegaPrime exposures it is found that our implementation correctly detects and masks more than 95% of all bright satellite tracks. The failures can mostly be traced to either dashed, non continuous satellite tracks or to short ones at the edges of the mosaic. We observed only a handful false-positive detections in very special configurations such as extended and bright object chains over chip boundaries. Pixels attached to identified tracks are set to zero in the corresponding weight maps.

A.3. Astrometric calibration

With the preprocessed Elixir images and the weight maps, the astrometric calibration of CARS data sets and the associated quality assessment follows very closely the procedures outlined in Sect. 5 of Erben et al. (2005):

1. SExtractor is used on all images to extract sources with at least 5 pixels having 5σ above the sky-background.
2. The Astrometrix programme (see Radovich 2002; McCracken et al. 2003) is run on the i' -band to determine a third order astrometric solution for each individual chip. We use the USNO-B1 standard-star catalogue (see

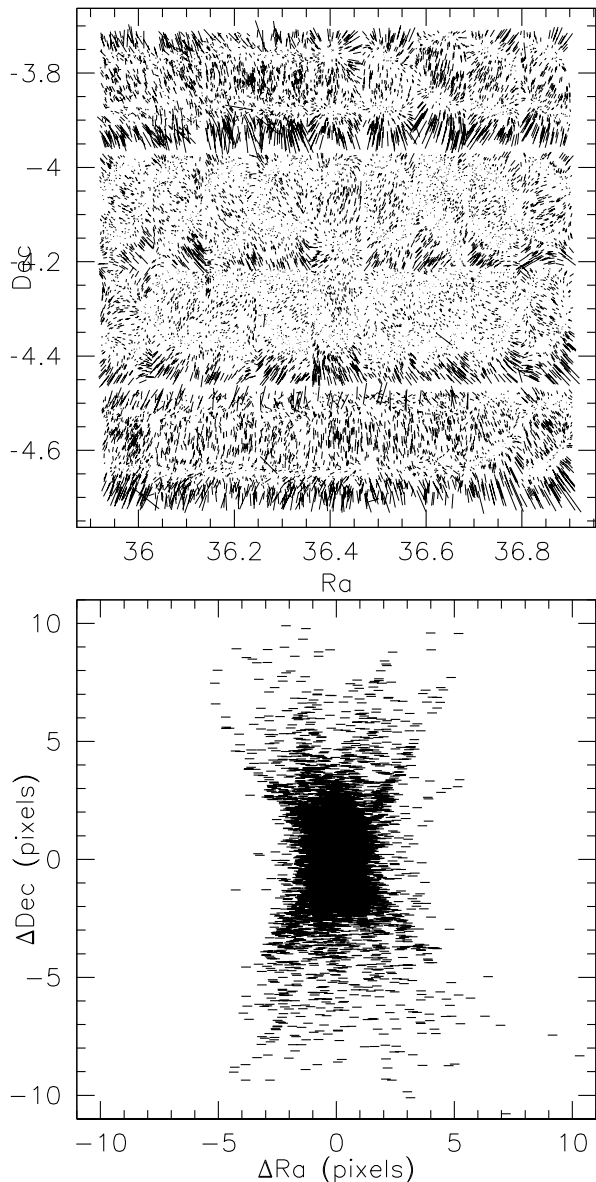


Fig. A.1. Higher order MegaPrime distortions: the plots show the difference in object position after a first-order astrometric alignment, i.e. corrections for linear shifts and rotations and a full third-order astrometric solution estimated by *Astrometrix*. The sticks in the upper plot indicate the positional displacement vector between the two solutions and the lower plot gives the absolute displacement numbers. We note that the second- and third-order terms contribute very significantly to the solution (see text for details).

Monet et al. 2003) as our astrometric reference frame. We co-add the i' -band data (see below) and extract a high S/N object catalogue (sources with at least 20 pixels of 20σ above the sky-background noise) from it. This catalogue is used as reference for the astrometric calibration of the $u^*g'r'z'$ data. It allows us to use a dense reference catalogue with high positional precision. This turned out to be essential to map robustly significant higher-order astrometric distortions of MegaPrime. For this instrument, the contributions of second- and third-order terms to the astrometric correction are up to $2''.0$. As a comparison, for the four times smaller WFI@MPG/ESO2.2m camera these values are on the order of $0''.5$; see also Fig. A.1. We use the i' -band data as reference because (1) the individual exposures are already

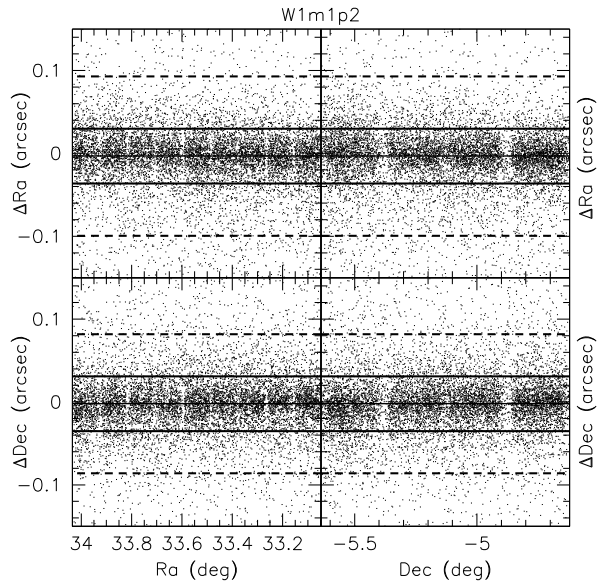


Fig. A.2. Internal Astrometric alignment of i' -band data from W1m1p2: shown are the differences of sources in 7 dithered i' -band observations after astrometric calibration with the counterparts in the co-added image. The 7 individual exposures were obtained with a dither pattern spanning about $45''.0$ in RA and $180''.0$ in Dec to cover the MegaPrime chip gaps. The plot covers the complete MegaPrime area of about 1 sq. degree. The thick solid lines mark the region containing 68% of all points and are at $\Delta RA = -0.003^{+0.029}_{-0.035}$ arcsec and $\Delta Dec = -0.002^{+0.031}_{-0.035}$ arcsec. Dashed lines show the corresponding area for 90% of all points ($\Delta RA = -0.003^{+0.092}_{-0.099}$ arcsec and $\Delta Dec = -0.002^{+0.081}_{-0.086}$ arcsec). Only 1 out of 10 points is shown for clarity of the plot.

reasonably deep and hence can be well calibrated with the USNO-B1 sources and (2) with seven dithered exposures the co-added i' -band typically has the best coverage and filling-factor of the MegaPrime area with its chip gaps in individual exposures.

3. For our scientific objectives, weak gravitational lensing, and multi-band studies with photometric redshifts it is essential to obtain a very high internal astrometric accuracy in the lensing band (i' in our case). As discussed in Erben et al. (2005) higher order object brightness-moments (everything above the zeroth order moment, i.e. the object flux) are significantly changed if individual frames of the WFI@MPG/ESO2.2m camera are aligned with an accuracy >0.5 pixel (pixel scale $0''.238$). For our CARS data we reach an accuracy of about $0''.03$ – $0''.04$, i.e. about 1/5th of a MegaPrime pixel. This was tested by comparing object positions (with $i'_{AB} < 20$) from astrometrically corrected individual frames with their cousins in the final co-added images. Results for the field W1m1p2 in the i' filter are shown in Fig. A.2. In a similar way the inter-colour alignment of different filters per pointing is tested. From the final co-added images we compare object positions of high S/N sources ($i'_{AB} < 20$). For all pointings we reach an alignment between the colours below one pixel. We note however that the inter-colour alignment between $g'r'i'$ is better (typically 0.5 pixels) than between $i'u^*z'$ (between 0.5 and 1 pixel). This is expected because individual frames from u^* and z' have fewer high S/N sources for astrometric calibration than the intermediate filter bands. We show results from the $i' - g'$ and $i' - u^*$ comparisons of W1m1p2 in Fig. A.3.

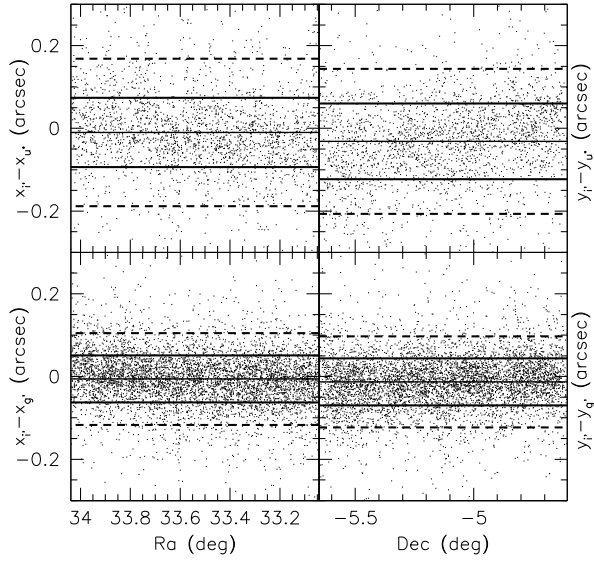


Fig. A.3. Astrometric alignment of different colours of CARS field W1m1p2: we show differences in object positions from different colours $u^*g'r'i'$ of the CARS pointing W1m1p2. The plot shows that the different bands are well aligned with sub-pixel accuracy although slight trends in the residuals with u^* are visible. Solid (dashed) lines enclose areas containing 68% (90%) of all points. They are at $x_r - x_{g'} = -0.006^{+0.05}_{-0.06} {}^{+0.10}_{-0.11}$ arcsec, $y_r - y_{g'} = -0.012^{+0.04}_{-0.07} {}^{+0.09}_{-0.12}$ arcsec and $x_r - x_{u^*} = -0.009^{+0.07}_{-0.09} {}^{+0.16}_{-0.18}$ arcsec, $y_r - y_{u^*} = -0.03^{+0.06}_{-0.12} {}^{+0.14}_{-0.20}$ arcsec. See text for further details.

A.4. Photometric calibration

The Elixir preprocessed images come with all necessary meta-data to translate pixel counts to instrumental AB magnitudes; see <http://www.cfht.hawaii.edu/Science/CFHTLS-DATA/megaprimecalibration.html#P2> for a full description of the Elixir procedures to derive photometric parameters. In addition, the CFHTLS exposure catalogue contains a flag whether an image was taken under photometric sky conditions or not. With this information we try to derive a photometric zeropoint for each colour of each pointing (we call this a set in the following) with the two-stage process described in Hildebrandt et al. (2006). If not stated otherwise, our photometric calibration and all photometric comparisons described in this Appendix are done with SExtractor MAG_AUTO magnitude estimates derived separately from each colour in each pointing.

1. We use Photometric to bring all individual images to the same flux scale by estimating the magnitude differences of overlap sources. This gives us for each image i a relative zeropoint $ZP_{rel,i}$ which tells us the magnitude offset of that image w.r.t. the mean relative zeropoint of all images, i.e. we demand $\sum_i ZP_{rel,i} = 0$. Note that this procedure relatively calibrates data obtained under photometric and non-photometric conditions. An absolute flux scaling can now be obtained from the photometric subset.
2. For images being observed under photometric conditions we calculate a corrected zeropoint $ZP_{corr,j}$ according to $ZP_{corr,j} = ZP + am \cdot ext + ZP_{rel,j}$, where am is the airmass during observation, ZP the instrumental AB zeropoint and ext the colour dependent extinction coefficient. The last two quantities are part of the provided Elixir meta-data. For images obtained under photometric conditions, the relative zeropoints compensate for atmospheric extinction and the corrected zeropoints agree within measurement errors in

the ideal case. We later use the mean $\langle ZP_{corr,j} \rangle$ as zeropoint for our co-added images.

Note that we can determine an absolute zeropoint only if at least one exposure of a given set was obtained under photometric conditions. For the CARS data this is not the case for 12 sets and we estimated a zeropoint for those after image co-addition by flux comparison with objects of adjacent, calibrated pointings. As discussed in Hildebrandt et al. (2006) the corrected zeropoints offer a good opportunity to verify the quality of absolute photometric calibration. If a field is observed over an extended period, the comparison of zeropoints estimated from different nights gives a robust indication on the long-term stability of photometric instrument properties and on the calibration process itself.

However, the CARS fields from the CFHTLS-Wide Survey were observed mostly in a compact period during a single night and hence do not allow for this test directly. To perform this important quality control we consider observations of the CFHTLS-Deep Survey. This part of the CFHTLS continuously observes four one square degree fields with the goal to detect Supernovae and to measure their light curves; see Astier et al. (2006) for more details on this survey. Because we noticed severe problems with our u^* flux calibration for W3 and W4 later on (see Sect. A.6 below) we investigated CFHTLS-Deep images which were publicly available at 01/01/2008 and which had the photometric flag in the CFHTLS exposure catalogue. We studied the long-term evolution of the corrected zeropoints from June 2003 to December 2006. Results for the fields D1, D3 and D4 are shown in Fig. A.4. For the D1 area we studied in detail photometric stability in all five filter bands. Figure A.4 shows that the photometric calibration of this field over time is very consistent with formal standard deviations of only up to about 0.03 mag. Note however that the peak differences of magnitude zeropoints span more than 0.1 mag! For the u^* -band observations of D3 and D4 we observe a considerably larger scatter with extremely low values for the corrected zeropoints (too high CARS magnitude zeropoints) from around April 2006 to November 2006. This hints to a calibration problem of u^* -band CFHTLS data in that period and the data suggest a necessary correction of about -0.2 mag for u^* -band CARS observations from spring to fall 2006. Due to its visibility D1 has no observations in that period. We verified that the D4 results for the colours $g'r'i'z'$ are similar to those in D1 and hence the problem seems to be confined to u^* . These discrepancies in the u^* calibration are also documented in Gwyn (2008) and on TERAPIX WWW pages describing the official T0004 CFHTLS data release. (http://terapix.iap.fr/article.php?id_article=713).

The Deep data allow us also to check homogeneity and reproducibility of our photometric calibration over the MegaPrime field-of-view. In each colour we created three independent co-added images from D1. Each stack contains five images obtained under photometric conditions in November 2003, 2004 and 2005. From the different stacks in each colour we match bright ($17 < m < 20$) sources whose positions agree to 0".5 or better. Magnitudes are compared and mean offsets and standard deviations are estimated. Table A.1 summarises the results. Except for the z' -band the total magnitudes agree to better than 0.04 mag for these stacks. The scatter around these absolute offsets is around 0.02 mag for $u^*g'r'i'$ and about 0.03–0.04 mag for z' ; we attribute the higher value in z' to fringe residuals in this band. These values give us an estimate on the internal photometric accuracy of our data, i.e. on the error propagation of inaccuracies in our photometric calibration procedures to final magnitude

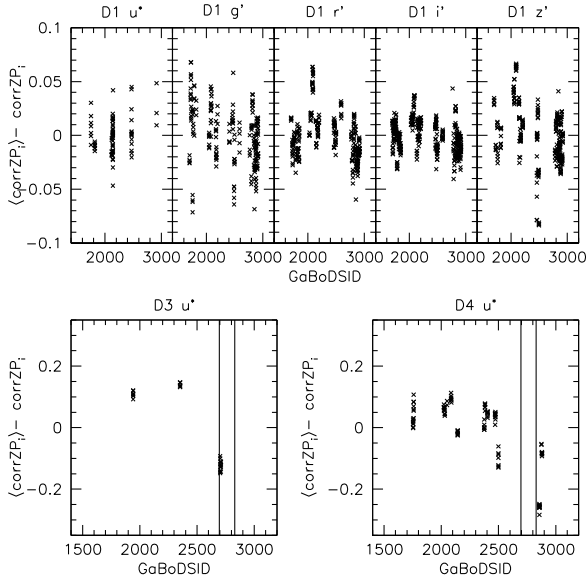


Fig. A.4. Long-term studies of corrected zeropoints in CFHTLS-Deep data: we analysed all publicly available photometric data from the CFHTLS-Deep fields D1 (RA: 02:26:00; Dec: $-04:30:00$; all colours), D3 (RA: 14:19:28; Dec: $+52:40:41$; u^* -band) and D4 (RA: 22:15:31; Dec: $-17:44:06$; u^* -band). The panels show the long-term evolution of corrected photometric zeropoints in these fields from 25/06/2003–29/12/2006. On the measured zeropoint distributions we performed an iterative 3σ clipping to exclude obvious outliers. The quoted GoBoDSID is a running number counting the nights from 31/12/1998. The vertical lines in the D3 and D4 panels show the period of W3 and W4 u^* observations for which we observe larger discrepancies in comparisons with SDSS magnitudes; see text for further details.

Table A.1. Comparison of magnitudes from three independent stacks of CFHTLS-Deep D1 data in each colour (upper row: stacks from 2003 vs. 2004; lower row: stacks from 2003 vs. 2005).

$\Delta u^* \times 100$	$\Delta g' \times 100$	$\Delta r' \times 100$	$\Delta i' \times 100$	$\Delta z' \times 100$
-3.3 ± 1.8	1.3 ± 1.5	-0.5 ± 1.3	-1.4 ± 2.0	4.6 ± 3.1
-2.6 ± 2.0	3.3 ± 1.6	0.6 ± 1.6	-0.0 ± 2.0	-7.3 ± 3.8

estimates. We consider them as upper limits because possible errors in the determination of the photometric superflat within Elixir contribute to the quoted numbers. We note that we obtain consistent errors when comparing the Deep stacks with the CARS pointing W1p2p3. Their distance on the sky is $5'.0$ in RA, $18'.0$ in Dec and we can compare fluxes from objects which fall in different areas of the MegaPrime mosaic. The test between the Deep stack from 2003 and W1p2p3 yields: $\Delta u^* = 0.003 \pm 0.022$ mag; $\Delta g' = 0.014 \pm 0.014$ mag; $\Delta r' = 0.053 \pm 0.012$ mag; $\Delta i' = -0.019 \pm 0.014$ mag; $\Delta z' = -0.034 \pm 0.034$ mag.

A.5. Image co-addition

After the photometric calibration we check whether the individual exposures of a given set were obtained under varying photometric conditions which is indicated by a large range of relative zeropoints. Low-value outliers point to images which were observed under unfavourable sky-conditions w.r.t. the rest of the set. We estimate the median $med(ZP_{rel,i})$ of the relative zeropoint distribution and sort out exposures with a relative zeropoint of $med(ZP_{rel,i}) - 0.1$ or smaller. Affected are the five CARS sets W1p1p2- i' , W1p3m0- i' , W1p4m0- i' , W4m1m1- z' and W4m1m2- z' . At this stage we also reject short calibration exposures ($t_{exp} < 100$ s) from further processing.

Finally the exposures belonging to a set are sky-subtracted with SExtractor and co-added with the Swarp programme (see Bertin 2008). We use the LANCZOS3 kernel to remap original image pixels according to our astrometric solutions. The subsequent co-addition is done with a statistically optimal weighted mean which takes into account sky-background noise, weight maps and the relative photometric zeropoints as described in Sect. 7 of Erben et al. (2005). As sky projection we use the TAN projection (see Greisen & Calabretta 2002) and all colours from a specific pointing are mapped on the same pixel grid. The origins of the TAN projection for each pointing are those defined for the CFHTLS-Wide survey (see <http://terapix.iap.fr/cpl/oldSite/Descart/summarycftlswide.html>). An example for a final co-added image is shown in Fig. 2.

After co-addition we cut all images to a common size of $21k \times 21k$ which covers areas with useful data for all CARS pointings. We visually check each product for obvious defects. Because no pixel rejection takes place in our weighted mean stacking the co-added images show some remaining artefacts. We observe faint satellite tracks which were not detected and removed by our automatic satellite track masking tool (see Sect. A.2), short asteroid trails and warm pixels. Within the subsequent catalogue creation process we tried to mask these defects on the basis of the i' -band of each pointing (see Sect. 3).

A first rough check for the photometric calibration of each co-added image is done with the help of galaxy number counts. In all colours we estimated reference counts from the CFHTLS D1 field and compare those to our CARS Wide data. The reference counts are about two magnitudes deeper than those from our co-added images. Each of the one square degree fields yields a robust estimation of these counts and allows us to quickly spot photometric calibrations with obvious problems ($\Delta m \approx 0.2$ mag). Galaxies are selected by the SExtractor CLASS_STAR parameter ($CLASS_STAR < 0.95$); see Fig. A.5 for an example of the field W1p2p2. With multi-colour observations for all fields we also can compare colours from stellar sources with predictions from the Pickles (1998) library. We select bright, unsaturated stars by magnitude ($17 < i'_{AB} < 22$) and by $CLASS_STAR > 0.95$. With data in $u^*g'r'i'z'$ we plot ten possible colour-colour combinations against the Pickles stellar library (Pickles 1998) which allows us, similar to the galaxy number counts, to identify grossly inaccurate zeropoints with $\Delta m \approx 0.1-0.2$ mag. See Fig. A.6 for an example track of W1p2p2.

A much more rigorous and accurate test for the photometric quality of our data is given by direct comparison with external and well calibrated data sets. This is the topic of the following sections.

A.6. Comparison of CARS data with SDSS photometry

The overlap of all three CARS patches with the SDSS (see Sect. 2) allows us a direct comparison of object fluxes with Sloan photometry. To convert the instrumental MegaPrime AB magnitudes from stellar objects to the SDSS system we use the following transformation formulae:

$$\begin{aligned}
 u_{AB}^* &= u_{SDSS} - 0.241 \cdot (u_{SDSS} - g_{SDSS}) \\
 g_{AB}' &= g_{SDSS} - 0.153 \cdot (g_{SDSS} - r_{SDSS}) \\
 r_{AB}' &= r_{SDSS} - 0.024 \cdot (g_{SDSS} - r_{SDSS}) \\
 i_{AB}' &= i_{SDSS} - 0.085 \cdot (r_{SDSS} - i_{SDSS}) \\
 z_{AB}' &= z_{SDSS} + 0.074 \cdot (i_{SDSS} - z_{SDSS})
 \end{aligned} \tag{A.1}$$

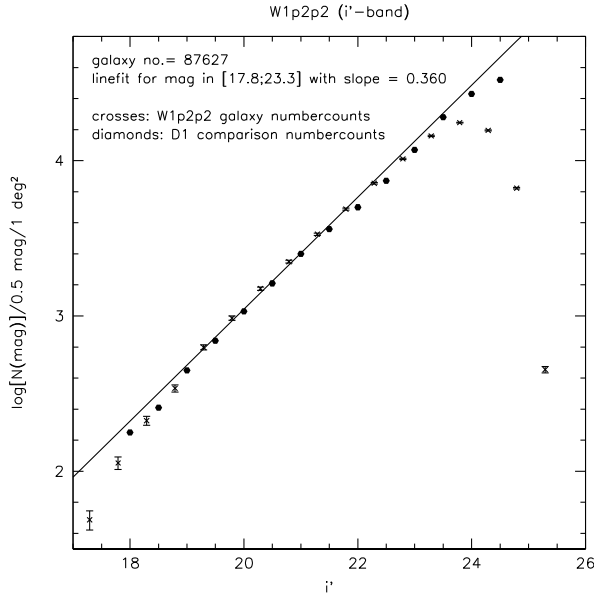


Fig. A.5. i' -band numbercounts for the field W1p2p2: galaxies are selected with $\text{CLASS_STAR} < 0.95$ to allow for a first crude check of our magnitude zeropoints with galaxy-number counts.

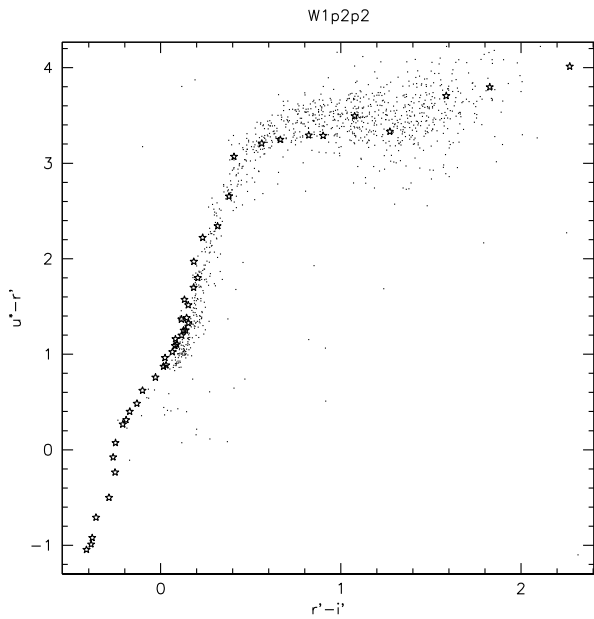


Fig. A.6. $u^* - r''$ vs. $r' - i''$ colour–colour diagram in the field W1p2m2. The dots represent the measured colours of stars ($\text{SExtractor CLASS_STAR} > 0.95$ and $i'_{\text{AB}} < 20$; $N = 1089$) and the star symbols are colours of stars from the library of Pickles (1998).

The relations for $g'r'i'z'$ were determined within the CFHTLS-Deep Supernova project (see <http://www.astro.uvic.ca/~pritchet/SN/Calib/ColourTerms-2006Jun19/index.html#Sec04>); the u^* transformation comes from the CFHT instrument page (see <http://cfht.hawaii.edu/Instruments/Imaging/MegaPrime/generalinformation.html>).

For all the following photometric comparison studies we extracted *single frame* photometric catalogues from all CARS images and we use the $\text{SExtractor MAG_AUTO}$ estimate throughout, i.e. here we do not use the multi-colour catalogues described in Sect. 3. We compare magnitude estimates from sources

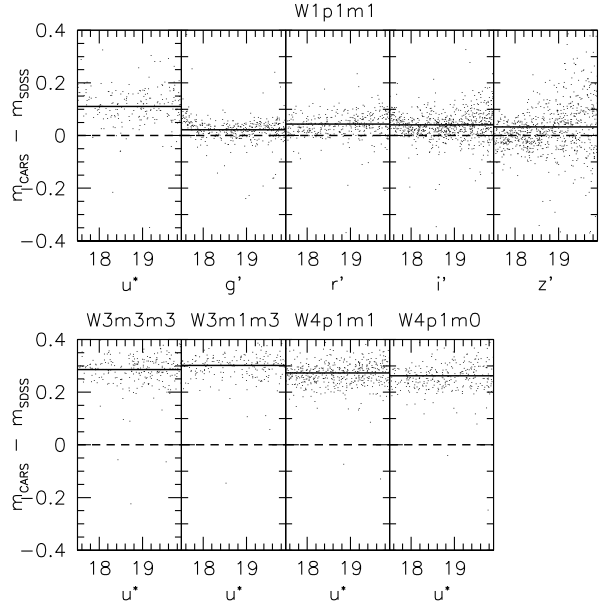


Fig. A.7. Comparison of CARS fluxes and SDSS magnitudes: we show magnitude offsets of CARS data with SDSS overlap. The upper row shows the comparison for all five bands of the field W1p1m1. The dashed line in the plots indicates the zero offset and the solid line the observed mean difference; see text for a discussion of the results.

classified as stars in the SDSS and having a CARS MAG_AUTO estimate of $17 < m < 20$. Representative results of our SDSS comparisons are shown in Fig. A.7. A complete listing of the measured magnitude offsets and dispersions can be found in Table A.2. We note a stable calibration in $g'r'i'$. For nearly all fields the mean offset in these filters is well below 0.05 mag and the transformation relations from Eq. (A.1) are valid with $\sigma_{g',r',i'} \approx 0.02\text{--}0.04$ mag in the magnitude range $17 < m < 20$. For z' the mean offset reaches up to 0.08 mag and also the dispersion broadens to $\sigma_{z'} \approx 0.04\text{--}0.07$ mag. Larger disagreements are observed for the u^* filter. For the three W1 fields with SDSS overlap we measure a consistent offset of $u^* - u_{\text{SDSS}} + 0.241 \cdot (u_{\text{SDSS}} - g_{\text{SDSS}}) \approx 0.1$. Two of the u^* fields (W1p3m0 and W1p4m0) were observed on 01/01/2006 and 02/01/2006 and the third one, W1p1m1, on 13/12/2006 and hence we obtain this result for different calibration periods. Our long-term zeropoint analysis of D1 for which u^* -band data have been obtained during December 2006 does not indicate larger systematic calibration offsets. Hence, at the current stage, we have no explanation for this high, consistent offset between our W1 u^* fluxes and the SDSS magnitudes. Even considerably larger absolute offsets (up to 0.3 mag) are observed for all CARS u^* pointings of W3 and W4. However, as was discussed in Sect. A.4 systematic zeropoint offsets for the u^* calibration are observed from April 2006 to November 2006 and all W3 and W4 u^* band observations were obtained just in that period. The data presented in Fig. A.4 suggest a necessary correction for the u^* -band zeropoint of about 0.2 mag which would make the observed offsets consistent with the W1 results. For u^* , the dispersion with the transformation in Eq. (A.1) is about $\sigma_{u^*} \approx 0.03\text{--}0.06$ mag ($17 < u^* < 20$).

A.7. Photometric comparison of CARS images with publicly available CFHTLS data

We further check the quality of our photometric calibration by comparison with publicly available CFHTLS data. We

use the TERAPIX T0003 data release¹² (see http://www1.cadc-ccda.hia-ihp.nrc-cnrc.gc.ca/cadcbn/cfht/wdbi.cgi/cfht/tpx_fields/form and http://terapix.iap.fr/rubrique.php?id_rubrique=208) which consists of all available CFHTLS-Deep and CFHTLS-Wide observations until 12/09/2005. It overlaps with our data on 24 sq. degrees with the full five-colour coverage on nine sq. degrees. Furthermore, Stephen Gwyn considers public CFHTLS data within his MegaPipe project which aims at providing calibrated and co-added data from the complete MegaPrime archive at CADC (see Gwyn 2008). At the time of writing the MegaPipe project overlaps with CARS on 22 sq. degrees with five-colour coverage on two sq. degrees. All three projects start their processing from the Elixir images but each pipeline derives the photometric calibration with different software modules and by including different internal and external data sets. Hence, this comparison gives us another check on the accuracy and limitations of our algorithms:

- The T0003 data are processed on a patch basis, i.e. to derive a photometric solution all available information from a CFHTLS-Wide patch are considered simultaneously. The global photometric analysis takes into account overlap sources from adjacent pointings and also allows modest variations of the derived Elixir zeropoints to better ensure a consistent solution on the complete patch. In contrast, the CARS data are treated on a strict pointing-by-pointing basis. Other differences in the processing which might influence direct flux comparisons between T0003 and CARS are:
 1. To select suitable Elixir images for further processing TERAPIX does not rely solely on the quality flag in the CFHTLS exposure catalogue but each image is regraded. Hence, the composition of image stacks might be different for some pointing/colour combinations. We did not investigate this in detail.
 2. The T0003 stacks are created with a median co-addition whereas CARS uses a weighted mean statistics. Satellite tracks in individual frames are not masked before co-addition in the T0003 processing.
- The MegaPipe project directly uses the SDSS to photometrically calibrate MegaPrime data on a pointing basis. For observations which overlap with Sloan, the relations from Eq. (A.1) are used to derive zeropoints for the images. For observations outside the Sloan area, the procedure is similar to ours. If data are obtained under photometric conditions, the Elixir calibration is used. Otherwise, a calibration with adjacent pointings having photometric information is tried. Similar to the T0003 processing all MegaPipe images are rechecked manually for their suitability to be processed further and the final stacking is done with a median co-addition.

The results of our flux comparisons with 93 T0003 and 62 MegaPipe fields are detailed in Table A.2.

We note in general a very good agreement between our calibration and that from TERAPIX T0003. For all but four pointings the discrepancy is less than 0.04 mag. Notable differences occur for the stacks W1p2p3- r' ($m_{\text{CARS}} - m_{\text{T0003}} = -0.063$ mag), W1m1p3- u^* ($m_{\text{CARS}} - m_{\text{T0003}} = -0.18$ mag), W1m1p3- z' ($m_{\text{CARS}} - m_{\text{T0003}} = -0.12$ mag) and W1m1p2- u^* ($m_{\text{CARS}} - m_{\text{T0003}} = -0.12$ mag). As discussed in Sect. A.4 the field W1p2p3 overlaps with CFHTLS-Deep 1 and we can confirm an offset of about 0.05 mag between the CARS W1p2p3- r'

stack and corresponding Deep data. All four individual images contributing to the CARS image have been obtained under photometric conditions which is confirmed by a very narrow distribution (about 0.01 mag) of relative zeropoints. At the current stage we do not have a conclusive explanation for the observed discrepancy in this field. We note that W1p4p3- r' for which we observe no discrepancy ($m_{\text{CARS}} - m_{\text{T0003}} = -0.007$ mag) has been observed in the same night (23/08/2003) as W1p2p3- r' . Furthermore, these two sets share the same photometric calibration data.

For the other three cases with a fairly large magnitude shift of more than 0.1 mag all the science frames were obtained under non-photometric conditions with a flux absorption of about 0.2 mag which probably leads to larger errors in the estimation of fluxes and relative zeropoints. The images were absolutely calibrated with one short exposed image obtained under photometric conditions.

The direct comparison of CARS and the MegaPipe images shows considerably larger scatters. We investigated in more detail the case of MegaPipe W3m1m2- r' which shows a magnitude offset of nearly 0.1 mag w.r.t. CARS, T0003 and the SDSS. It turned out that an image obtained under unfavourable photometric conditions was included in the calibration and stacking process although it should have been rejected. The median-stacking of heterogeneous data (MegaPipe does, by default, not reject very short calibration exposures as CARS and T0003) and problematic images that slipped through the grading process probably account for the observed scatters in other cases (Gwyn, private communication).

A.8. Photometric accuracy of CARS data – summary

In the preceding sections we evaluated the internal and external photometric quality of our data. The results can be summarised as follows:

- We evaluated the internal photometric accuracy of our co-added data with observations from the CFHTLS-Deep survey. From D1 we constructed in each colour three independent stacks which contain data from 2003, 2004 and 2005 and compared fluxes from overlap sources. The CARS set W1p2p3 which was obtained in 2003 and is offset to D1 is included in these tests. Around some absolute offsets, the magnitude comparisons show internal scatters with $\sigma_{\text{int},u^*g'r'i'} \approx 0.01\text{--}0.02$ mag in $u^*g'r'i'$ and about $\sigma_{\text{int},z'} \approx 0.03\text{--}0.04$ mag in z' and we quote these values as internal magnitude uncertainties over the MegaPrime field-of-view.
- The accuracy of the absolute photometric calibration is primarily tested with a comparison to the Sloan Digital Sky Survey. The available Elixir pre-calibration allows us to obtain an absolute photometric accuracy of about $\sigma_{\text{abs},g'r'i'} \approx 0.01\text{--}0.04$ mag in the $g'r'i'$ bands. Unbiased results are also obtained for z' with an accuracy of $\sigma_{\text{abs},z'} \approx 0.03\text{--}0.05$ mag. At the current stage we obtain a systematic bias of about 0.1 mag for the u^* -band. This holds directly for our data in W1. For W3 and W4 we arrive at the same conclusion if we take into account systematics revealed by our zeropoint study of CFHTLS-Deep data. Given this result we quote the zeropoint uncertainty in the u^* -band with $\sigma_{\text{abs},u^*} \approx 0.15$ mag.
- Because we process our data on a pointing basis we also need to calibrate our images set by set relying on Elixir metadata only. We generally do not take into account information from adjacent pointings. TERAPIX T0003 data are treated with a more sophisticated procedure using all available

¹² At the time of writing the most recent TERAPIX T0004 release (with a 35 sq. degree five-colour CARS overlap) was not publicly available.

Table A.2. CARS data quality overview; see the text for details.

Field/Area ^a [sq. deg.]	Filter	<i>N</i>	expos. time [s]	<i>m</i> _{lim} [AB mag]	Sloan ^b $\Delta m \times 100$	T3/MegaP. ^c $\Delta m \times 100$	seeing [$''$]	comments
W1m0p1 [w1.-0+1] (0.84)	<i>u</i> [*]	5	3000.51	25.27	–	0.0 ± 0.8 (T)	1.00	
	<i>g</i> '	5	2500.45	25.55	–	–0.4 ± 1.3 (M) –0.4 ± 0.5 (T) –7.1 ± 0.9 (M)	0.90	
	<i>r</i> '	3	1500.28	24.72	–	–1.9 ± 1.0 (T)	0.79	
	<i>i</i> '	7	4305.67	24.61	–	–0.1 ± 0.8 (T) –0.8 ± 0.7 (M)	0.85	
	<i>z</i> '	11	6601.19	23.88	–	0.2 ± 1.5 (T) –7.7 ± 1.1 (M)	0.79	
W1m0p2 [w1.-0+2] (0.76)	<i>u</i> [*]	5	3000.58	25.35	–	–0.6 ± 1.1 (T) –2.2 ± 1.5 (M)	1.00	
	<i>g</i> '	7	3500.46	25.72	–	–0.5 ± 1.0 (T) –2.5 ± 0.9 (M)	0.95	
	<i>r</i> '	2	1000.18	24.61	–	–0.5 ± 0.5 (T)	0.82	no ch. 21, 35
	<i>i</i> '	7	4305.66	24.72	–	1.3 ± 2.4 (T) 0.2 ± 1.8 (M)	0.74	
	<i>z</i> '	10	6000.83	23.64	–	–1.2 ± 3.5 (T) –7.3 ± 1.5 (M)	0.79	fr. res.
W1m0p3 [w1.-0+3] (0.75)	<i>u</i> [*]	5	3000.58	25.27	–	–1.0 ± 1.4 (T) 5.3 ± 1.2 (M)	0.87	
	<i>g</i> '	5	2500.49	25.56	–	–0.7 ± 0.8 (T) –1.9 ± 0.6 (M)	0.90	
	<i>r</i> '	2	1000.18	24.62	–	–1.2 ± 0.5 (T)	0.85	no ch. 21, 35
	<i>i</i> '	7	4305.65	24.59	–	–0.5 ± 0.7 (T) –0.8 ± 0.5 (M)	0.74	
	<i>z</i> '	10	6000.84	23.59	–	–1.3 ± 2.7 (T) –8.1 ± 1.4 (M)	0.82	fr. res.
W1m1p1 [w1.-1+1] (0.84)	<i>u</i> [*]	7	4200.60	25.50	–	–	1.00	
	<i>g</i> '	8	4000.76	25.73	–	–	0.66	
	<i>r</i> '	2	1000.20	24.51	–	–	0.59	
	<i>i</i> '	9	5535.73	24.53	–	–	0.79	
	<i>z</i> '	6	3600.40	23.30	–	–	0.75	
W1m1p2 [w1.-1+2] (0.82)	<i>u</i> [*]	5	3000.52	25.03	–	–12.0 ± 0.6 (T) –9.2 ± 1.5 (M)	0.92	
	<i>g</i> '	5	2500.48	25.44	–	3.3 ± 0.7 (T) –4.1 ± 1.0 (M)	0.87	
	<i>r</i> '	4	2000.38	24.80	–	1.0 ± 2.2 (T) –2.1 ± 2.0 (M)	0.87	
	<i>i</i> '	7	4305.66	24.52	–	–0.1 ± 1.8 (T) 1.6 ± 2.1 (M)	0.71	
	<i>z</i> '	11	6601.18	23.87	–	–1.1 ± 1.5 (T) 0.3 ± 0.8 (M)	0.71	fr. res.
W1m1p3 [w1.-1+3] (0.76)	<i>u</i> [*]	5	3000.50	24.95	–	–18.3 ± 0.5 (T)	0.79	
	<i>g</i> '	3	1500.30	25.22	–	1.0 ± 0.8 (T)	0.77	
	<i>r</i> '	2	1000.23	24.58	–	1.4 ± 0.8 (T)	0.79	no ch. 21, 35
	<i>i</i> '	7	4305.70	24.58	–	–0.3 ± 1.0 (T)	0.74	
	<i>z</i> '	10	6001.00	23.43	–	–11.9 ± 2.3 (T)	0.71	fr. res.
W1p1m1 [w1.+1-1] (0.85)	<i>u</i> [*]	5	3000.42	25.26	12.2 ± 5.5	–	0.85	
	<i>g</i> '	6	3000.47	25.79	2.7 ± 2.8	–	0.87	
	<i>r</i> '	2	1000.16	24.50	4.2 ± 3.4	–	0.71	
	<i>i</i> '	7	4305.53	24.85	5.2 ± 4.8	–	0.71	
	<i>z</i> '	6	3600.40	23.52	1.3 ± 5.7	–	0.85	
W1p1p1 [w1.+1+1] (0.75)	<i>u</i> [*]	5	3000.47	25.28	–	0.6 ± 0.9 (T) 6.6 ± 0.7 (M)	0.92	
	<i>g</i> '	10	5000.88	25.97	–	–0.3 ± 0.7 (T) –2.0 ± 0.5 (M)	0.95	
	<i>r</i> '	2	1000.18	24.57	–	–1.6 ± 0.6 (T)	0.85	
	<i>i</i> '	7	4305.72	24.70	–	–0.1 ± 0.8 (T) –0.5 ± 0.5 (M)	0.82	
	<i>z</i> '	12	7201.21	23.94	–	0.9 ± 1.5 (T) –9.3 ± 1.3 (M)	0.74	fr. res.

Table A.2. continued.

Field/Area ^a [sq. deg.]	Filter	N	expos. time [s]	m_{lim} [AB mag]	Sloan ^b $\Delta m \times 100$	T3/MegaP ^c $\Delta m \times 100$	seeing ["]	comments
W1p1p2 [w1.+1+2] (0.83)	u^*	5	3000.48	25.29	–	-3.9 ± 1.0 (T)	1.00	
	g'	5	2500.42	25.60	–	-1.3 ± 1.0 (T)	0.87	
	r'	2	1000.16	24.50	–	-0.1 ± 0.6 (T)	0.74	
	i'	6	3690.57	24.45	–	-0.1 ± 1.0 (T)	0.77	
	z'	10	6001.00	23.60	–	-0.4 ± 1.8 (T)	0.63	fr. res.
W1p1p3 [w1.+1+3] (0.80)	u^*	5	3000.47	25.30	–	-2.7 ± 1.1 (T) -1.8 ± 1.7 (M)	0.95	no ch. 21, 35
	g'	5	2500.42	25.53	–	2.4 ± 0.8 (T)	0.95	no ch. 21, 35
	r'	4	2000.22	24.72	–	-1.4 ± 1.4 (T)	0.89	no ch. 21, 35
	i'	8	4920.84	24.63	–	-0.4 ± 0.8 (T)	0.95	no ch. 21, 35
	z'	10	6001.03	23.63	–	-0.9 ± 2.2 (T) -9.9 ± 1.7 (M)	0.69	no ch. 21, 35; fr. res.
	W1p2p1 [w1.+2+1] (0.84)	u^*	5	3000.53	25.32	–	-3.1 ± 1.4 (T)	1.00
g'		5	2500.45	25.56	–	-1.9 ± 1.1 (T)	1.00	no ch. 31
r'		2	1000.18	24.42	–	-2.8 ± 0.6 (T)	0.95	no ch. 31
i'		8	4960.74	24.63	–	0.6 ± 0.6 (T)	0.90	no ch. 31
z'		10	6000.82	23.74	–	-0.9 ± 2.2 (T)	0.71	no ch. 31; fr. res.
W1p2p2 [w1.+2+2] (0.81)	u^*	5	3000.56	25.21	–	-2.8 ± 1.1 (T)	0.98	no ch. 21, 35
	g'	5	2500.45	25.63	–	1.4 ± 1.2 (T)	0.95	
	r'	2	1000.18	24.53	–	-3.4 ± 0.6 (T)	0.95	
	i'	8	4960.76	24.80	–	0.7 ± 1.1 (T)	0.85	
	z'	10	6000.95	23.73	–	-1.1 ± 1.3 (T)	0.74	
W1p2p3 [w1.+2+3] (0.83)	u^*	7	5950.29	25.61	–	-0.9 ± 0.5 (T)	1.00	no ch. 31
	g'	5	2500.35	25.62	–	-0.3 ± 0.5 (T)	0.95	
	r'	4	2000.37	24.82	–	-6.3 ± 0.9 (T)	0.71	
	i'	7	4340.55	24.59	–	-0.4 ± 0.9 (T)	0.95	
	z'	9	7200.41	23.80	–	0.9 ± 2.3 (T)	0.69	no ch. 31; fr. res.
W1p3m0 [w1.+3-0] (0.81)	u^*	5	3000.55	25.17	11.9 ± 6.6	6.4 ± 2.2 (M)	0.63	no ch. 31
	g'	5	2500.43	25.54	-1.8 ± 3.0	-2.6 ± 0.6 (T)	0.87	no ch. 31; m. ZP
	r'	2	1000.17	24.33	2.4 ± 3.0	0.1 ± 1.3 (T)	0.69	no ch. 31
	i'	5	3100.23	24.44	3.5 ± 3.5	3.1 ± 1.0 (T)	0.71	no ch. 31; sat. tr.
	z'	12	7201.49	23.59	-0.4 ± 7.2	-8.8 ± 3.7 (M)	0.71	no ch. 31; fr. res.
W1p3p1 [w1.+3+1] (0.85)	u^*	5	3000.26	25.31	–	–	0.85	no ch. 31
	g'	6	3000.27	25.62	–	0.0 ± 0.5 (T)	0.95	no ch. 31
	r'	2	1000.10	24.39	–	0.5 ± 0.7 (T)	0.85	no ch. 31
	i'	7	4340.32	24.60	–	-0.8 ± 1.1 (T)	0.95	no ch. 31
	z'	6	3600.47	23.55	–	–	0.69	no ch. 31
W1p3p2 [w1.+3+2] (0.82)	u^*	7	4200.42	25.45	–	5.0 ± 1.5 (M)	0.90	no ch. 31
	g'	5	2500.41	25.54	–	0.3 ± 0.9 (T)	0.85	no ch. 31; m. ZP
	r'	3	1500.22	24.51	–	-1.2 ± 1.2 (T)	0.83	no ch. 31
	i'	6	3720.24	24.48	–	0.6 ± 0.8 (T)	0.69	no ch. 31
	z'	6	3600.58	23.31	–	-7.3 ± 0.9 (M)	0.55	no ch. 31
W1p3p3 [w1.+3+3] (0.84)	u^*	4	2400.39	25.01	–	3.8 ± 0.9 (M)	1.11	no ch. 31
	g'	5	2500.20	25.51	–	0.1 ± 0.8 (T)	0.95	no ch. 31
	r'	2	1000.10	24.39	–	-2.9 ± 0.6 (T)	0.87	no ch. 31
	i'	7	4340.33	24.51	–	-1.3 ± 0.9 (T)	0.82	no ch. 31
	z'	6	3600.62	23.39	–	-7.2 ± 0.9 (M)	0.55	no ch. 31
W1p4m0 [w1.+4-0] (0.82)	u^*	5	3000.54	25.35	9.4 ± 4.7	6.4 ± 0.7 (M)	0.72	no ch. 31
	g'	5	2500.41	25.50	-1.5 ± 3.1	-0.8 ± 1.1 (T)	0.87	no ch. 31; m. ZP
	r'	2	1000.19	24.33	2.7 ± 2.5	0.3 ± 0.6 (T)	0.71	no ch. 31
	i'	4	2480.15	24.15	0.1 ± 3.1	0.9 ± 1.1 (T)	0.95	no ch. 31
	z'	6	3600.72	23.48	0.4 ± 5.9	-7.1 ± 0.8 (M)	0.69	no ch. 31
W1p4p1 [w1.+4+1] (0.82)	u^*	5	3000.54	25.42	–	–	0.79	
	g'	5	2500.43	25.45	–	-1.5 ± 0.7 (T)	0.85	no ch. 31; m. ZP
	r'	2	1000.16	24.21	–	1.6 ± 0.6 (T)	0.79	m. ZP
	i'	7	4340.62	24.48	–	0.3 ± 0.8 (T)	0.79	m. ZP
	z'	6	3600.52	23.34	–	–	0.63	
W1p4p2 [w1.+4+2] (0.87)	u^*	5	3000.60	25.29	–	–	0.77	
	g'	5	2500.44	25.49	–	-0.9 ± 1.3 (T)	0.85	no ch. 31; m. ZP
	r'	2	1000.16	24.22	–	-2.2 ± 0.8 (T)	0.74	m. ZP
	i'	7	4340.64	24.44	–	-0.9 ± 1.1 (T)	0.87	m. ZP
	z'	6	3600.50	23.45	–	–	0.55	

Table A.2. continued.

Field/Area ^a [sq. deg.]	Filter	<i>N</i>	expos. time [s]	<i>m</i> _{lim} [AB mag]	Sloan ^b $\Delta m \times 100$	T3/MegaP. ^c $\Delta m \times 100$	seeing ["]	comments
W1p4p3 [w1.+4+3] (0.83)	<i>u</i> [*]	5	3000.25	25.32	–	5.9 ± 0.8 (M)	0.98	no ch. 31
	<i>g</i> '	5	2500.41	25.65	–	-0.9 ± 2.3 (T)	0.95	no ch. 31
	<i>r</i> '	2	1000.17	24.46	–	-1.4 ± 1.1 (M)	–	–
	<i>i</i> '	7	4340.34	24.44	–	-0.7 ± 1.0 (T)	0.93	no ch. 31
	<i>z</i> '	6	3600.38	23.29	–	-1.0 ± 0.7 (T)	0.95	no ch. 31
W3m1m2 [w3.-1-2] (0.83)	<i>u</i> [*]	5	3000.96	24.78	30.2 ± 3.9	25.9 ± 2.5 (M)	0.87	–
	<i>g</i> '	5	2501.02	25.48	0.2 ± 1.9	0.2 ± 0.6 (T)	0.87	m. ZP
	<i>r</i> '	2	1000.47	24.51	-0.1 ± 2.7	-4.9 ± 1.5 (M)	0.63	–
	<i>i</i> '	7	4306.47	24.36	0.6 ± 3.8	-1.3 ± 0.7 (T)	0.66	–
	<i>z</i> '	6	3601.20	23.41	-6.1 ± 4.2	-9.9 ± 3.7 (M)	0.67	–
W3m1m3 [w3.-1-3] (0.82)	<i>u</i> [*]	5	3000.98	24.87	29.9 ± 3.8	26.9 ± 2.6 (M)	0.74	no ch. 21
	<i>g</i> '	5	2500.90	25.63	0.4 ± 2.0	0.1 ± 0.5 (T)	0.87	no ch. 21; m. ZP
	<i>r</i> '	2	1000.28	24.52	2.9 ± 2.2	-4.7 ± 1.1 (M)	0.97	no ch. 21
	<i>i</i> '	7	4306.61	24.36	0.6 ± 2.7	-2.2 ± 1.6 (M)	0.66	no ch. 21; m. ZP
	<i>z</i> '	6	3601.17	23.36	-3.8 ± 5.6	0.3 ± 0.9 (T)	0.59	no ch. 21
W3m2m2 [w3.-2-2] (0.85)	<i>u</i> [*]	5	3001.06	25.33	29.4 ± 4.1	25.3 ± 2.2 (M)	0.77	–
	<i>g</i> '	5	2500.89	25.59	0.7 ± 2.2	-0.3 ± 0.5 (T)	0.90	–
	<i>r</i> '	2	1000.42	24.56	0.7 ± 2.7	-3.8 ± 1.0 (M)	0.57	–
	<i>i</i> '	7	4306.23	24.46	0.3 ± 2.7	-1.1 ± 1.0 (T)	0.66	–
	<i>z</i> '	6	3601.22	23.43	-3.3 ± 4.9	-4.8 ± 2.2 (M)	0.64	–
W3m3m2 [w3.-3-2] (0.84)	<i>u</i> [*]	5	3000.99	25.27	29.0 ± 5.0	–	0.68	–
	<i>g</i> '	5	2500.87	25.40	0.4 ± 2.2	-0.2 ± 1.1 (T)	0.66	–
	<i>r</i> '	2	1000.40	24.20	4.5 ± 2.4	1.9 ± 0.7 (T)	0.66	–
	<i>i</i> '	7	4306.27	24.43	0.1 ± 3.3	0.0 ± 0.9 (T)	0.53	–
	<i>z</i> '	6	3601.20	23.30	-2.3 ± 4.7	–	0.55	–
W3m3m3 [w3.-3-3] (0.83)	<i>u</i> [*]	5	3001.02	25.29	28.8 ± 4.1	–	0.74	–
	<i>g</i> '	5	2500.93	25.52	0.2 ± 2.3	-0.5 ± 0.6 (T)	0.82	–
	<i>r</i> '	2	1000.42	24.25	4.4 ± 2.6	1.4 ± 0.6 (T)	0.66	–
	<i>i</i> '	7	4306.19	24.49	-0.8 ± 3.0	0.1 ± 0.8 (T)	0.50	–
	<i>z</i> '	6	3601.21	23.49	-3.1 ± 5.5	–	0.58	–
W4m0m0 [w4.+0+0] (0.82)	<i>u</i> [*]	5	3000.26	25.38	26.4 ± 3.8	–	1.03	–
	<i>g</i> '	5	2500.40	25.43	-0.1 ± 2.0	-1.9 ± 0.6 (M)	0.79	–
	<i>r</i> '	3	1500.22	24.23	-0.2 ± 2.2	1.0 ± 0.6 (M)	0.61	–
	<i>i</i> '	7	4305.65	24.62	5.3 ± 3.3	–	0.71	–
	<i>z</i> '	12	7200.87	23.78	-2.3 ± 4.6	–	0.66	–
W4m0m1 [w4.+0-1] (0.83)	<i>u</i> [*]	5	3000.29	25.30	23.2 ± 4.0	–	0.74	–
	<i>g</i> '	10	5000.68	25.85	-0.2 ± 2.5	-7.7 ± 1.6 (M)	0.82	–
	<i>r</i> '	2	1000.10	24.30	1.7 ± 2.3	-5.4 ± 1.7 (M)	0.67	–
	<i>i</i> '	7	4305.36	24.62	-0.8 ± 3.0	–	0.56	–
	<i>z</i> '	6	3600.27	23.29	-3.2 ± 5.0	–	0.50	–
W4m0m2 [w4.+0-2] (0.81)	<i>u</i> [*]	5	3000.31	25.41	24.0 ± 4.5	–	0.71	–
	<i>g</i> '	10	5000.58	25.83	-0.3 ± 1.9	-6.2 ± 1.2 (M)	0.77	–
	<i>r</i> '	2	1000.10	24.28	2.1 ± 2.2	–	0.58	–
	<i>i</i> '	7	4305.58	24.77	0.7 ± 2.6	–	0.61	–
	<i>z</i> '	6	3600.34	23.62	-4.4 ± 4.1	–	0.63	–
W4m1m1 [w4.-1-1] (0.79)	<i>u</i> [*]	5	3000.24	25.26	24.2 ± 3.9	–	0.69	–
	<i>g</i> '	13	6500.96	26.00	2.9 ± 2.4	–	0.79	–
	<i>r</i> '	2	1000.16	24.32	1.4 ± 2.5	–	0.87	–
	<i>i</i> '	6	3690.44	24.62	-0.2 ± 3.2	–	0.71	–
	<i>z</i> '	5	3000.24	23.28	-1.2 ± 4.8	–	0.48	–
W4m1m2 [w4.-1-2] (0.82)	<i>u</i> [*]	6	3600.41	25.45	33.2 ± 8.1	–	0.66	–
	<i>g</i> '	5	2500.53	25.54	-1.8 ± 1.8	-7.6 ± 1.3 (M)	0.79	–
	<i>r</i> '	2	1000.15	24.34	2.9 ± 2.4	–	0.50	–
	<i>i</i> '	7	4305.43	24.60	1.8 ± 2.9	–	0.72	–
	<i>z</i> '	5	3000.38	23.37	-0.3 ± 4.7	–	0.51	–

Table A.2. continued.

Field/Area ^a [sq. deg.]	Filter	<i>N</i>	expos. time [s]	<i>m</i> _{lim} [AB mag]	Sloan ^b $\Delta m \times 100$	T3/MegaP. ^c $\Delta m \times 100$	seeing [$''$]	comments
W4p1m0	<i>u</i> *	5	3000.43	25.29	26.2 ± 4.1	–	0.90	
[w4.+1+0]	<i>g</i> '	5	2500.30	25.40	1.6 ± 2.1	–2.3 ± 0.6 (M)	0.67	
(0.75)	<i>r</i> '	2	1000.16	24.35	3.0 ± 2.2	–	0.94	
	<i>i</i> '	7	4305.52	24.31	0.4 ± 3.3	–	0.53	
	<i>z</i> '	6	3600.36	23.33	–5.0 ± 4.2	–	0.55	
W4p1m1	<i>u</i> *	5	3000.22	25.33	27.5 ± 3.8	–	0.85	
[w4.+1–1]	<i>g</i> '	5	2500.34	25.33	1.2 ± 2.0	–	0.83	
(0.80)	<i>r</i> '	2	1000.17	24.28	–0.8 ± 2.5	–	0.67	
	<i>i</i> '	14	8611.03	24.86	1.4 ± 3.7	–	0.66	
	<i>z</i> '	6	3600.33	23.35	–4.2 ± 4.7	–	0.63	
W4p1m2	<i>u</i> *	5	3000.39	25.15	12.7 ± 3.9	–	0.87	
[w4.+1–2]	<i>g</i> '	5	2500.31	25.37	0.9 ± 1.9	–4.9 ± 1.3 (M)	0.85	
(0.82)	<i>r</i> '	2	1000.10	24.34	1.7 ± 2.1	–	0.61	
	<i>i</i> '	7	4305.41	24.57	1.1 ± 3.4	–5.8 ± 1.1 (M)	0.71	
	<i>z</i> '	5	3000.48	23.12	–2.1 ± 5.0	–	0.53	
W4p2m0	<i>u</i> *	5	3000.31	25.24	28.2 ± 4.4	–	0.79	
[w4.+2–0]	<i>g</i> '	5	2500.47	25.30	–1.6 ± 2.4	–4.4 ± 1.6 (M)	0.74	
(0.77)	<i>r</i> '	2	1000.14	24.36	2.0 ± 2.3	–	0.63	
	<i>i</i> '	7	4305.53	24.68	0.0 ± 3.0	–	0.57	
	<i>z</i> '	6	3600.39	23.20	–4.9 ± 3.9	–	0.79	
W4p2m1	<i>u</i> *	5	3000.36	25.18	19.7 ± 3.7	14.5 ± 2.0 (M)	0.98	
[w4.+2–1]	<i>g</i> '	5	2500.39	25.45	–0.7 ± 1.9	–6.4 ± 1.1 (M)	0.85	
(0.80)	<i>r</i> '	2	1000.22	24.12	1.6 ± 2.4	–	0.85	
	<i>i</i> '	7	4305.69	24.53	–3.4 ± 2.9	–9.9 ± 0.9 (M)	0.66	
	<i>z</i> '	12	7200.72	23.77	–8.0 ± 4.5	–15.7 ± 2.1 (M)	0.74	
W4p2m2	<i>u</i> *	4	2400.24	25.18	16.4 ± 3.7	–	1.00	
[w4.+2–2]	<i>g</i> '	5	2500.37	25.36	–1.3 ± 2.1	–	0.77	
(0.83)	<i>r</i> '	2	1000.22	24.05	2.5 ± 2.5	–	0.90	
	<i>i</i> '	13	7995.87	24.98	1.9 ± 4.1	–	0.63	
	<i>z</i> '	10	6000.55	23.66	–3.7 ± 4.0	–	0.72	

^a The column contains: CARS field-naming convention, CFHTLS field-naming convention and effective field area after image masking.

^b We give $\Delta m = m_{\text{CARS}} - m_{\text{Sloan}}$.

^c The column lists magnitude comparisons of CARS fields with those from TERAPIX T0003 (indicated by (T)) and MegaPipe (indicated by (M)); we give $\Delta m = m_{\text{CARS}} - m_{\text{other}}$.

information to simultaneously calibrate data on a patch-wide basis. Our direct comparison shows that both pipelines lead to very comparable results with a small average magnitude scatter of about 0.02 mag. However, we observe four significant outliers (out of 93 common CARS-T0003 sets) with magnitude offsets of 0.05–0.18 mag. Unfortunately no other external comparison is available for these fields. If we take the conservative approach to attribute these offsets to inaccuracies in our calibration and if the current CARS data set is representative less than 5% of our images severely suffer from a non-optimal photometric calibration procedure.

A.9. Detailed CARS data quality information

In Table A.2 we provide detailed information on the characteristics of each CARS data set. It contains the effective area of each field after image masking (see Sect. 3.4), the number of individual images contributing to each stack, the total exposure time, the limiting magnitude as defined in Sect. 2, magnitude comparisons with Sloan, the TERAPIX T0003 and the MegaPipe releases as described in Sects. A.6 and A.7, the measured image seeing and special comments. The comments field lists notable defects originating from the data itself or from our reduction process. We do not list defects of astronomical origin (e.g. very bright stars, external reflections) or problems which are present in a large number of images (e.g. faint satellite tracks,

asteroid tracks, residual warm pixels, low-level fringe residuals which are visible in most of the *z*' images). We use the following abbreviations:

- **no ch. XX**: the stack contains no data around chip position(s) XX. We number the MegaPrime mosaic chip from left to right and from bottom to top. The lower left (east-south) chip has number 1, the lower right (west-south) chip number 9 and the upper-right (west-north) chip number 36. Note that this labeling scheme differs from that used at CFHT.
- **fr. res.**: the co-added image shows significant fringe residuals.
- **m. ZP**: the zeropoint for this image was obtained manually by comparing object fluxes from the image with adjacent, photometrically calibrated pointings; see Sect. A.4.
- **sat. tr.**: the co-added image shows a bright satellite track which was not masked by our track detection module.

References

- Adelman-McCarthy, J. K., Agüeros, M. A., Allam, S. S., et al. 2007, ApJS, 172, 634
- Astier, P., Guy, J., Regnault, N., et al. 2006, A&A, 447, 31
- Bahcall, N., & Fan, X. 1998, ApJ, 504, 1
- Bahcall, N. A., McKay, T. A., Annis, J., et al. 2003, ApJS, 148, 243
- Bartelmann, M., & Schneider, P. 2001, Phys. Rep., 340, 291
- Bender, R., Appenzeller, I., Böhm, A., et al. 2001, in Deep Fields, ed. S. Cristiani, A. Renzini, & R. E. Williams

- Benitez, N. 2000, *ApJ*, 536, 571
- Bertin, E. 2003, SExtractor v2.3 User's manual, <http://terapix.iap.fr/>
- Bertin, E. 2008, Swarp v2.17.0 User's guide, <http://terapix.iap.fr/>
- Bertin, E., & Arnouts, S. 1996, *A&AS*, 117, 393
- Bertin, E., & Marmo, C. 2007, Weightwatcher v1.8.6 User's guide <http://terapix.iap.fr/>
- Böhringer, H., Voges, W., Huchra, J. P., et al. 2000, *ApJS*, 129, 435
- Böhringer, H., Schuecker, P., Guzzo, L., et al. 2004, *A&A*, 425, 367
- Bolzonella, M., Miralles, J. M., & Pelló, R. 2000, *A&A*, 363, 476
- Borgani, S., & Guzzo, L. 2001, *Nature*, 409, 39
- Borgani, S., Rosati, P., Tozzi, P., & Norman, C. 1999, *ApJ*, 517, 40
- Boulade, O., Charlot, X., Abbon, P., et al. 2003, in *Instrument Design and Performance for Optical/Infrared Ground-based Telescopes*, ed. M. Iye, & A. F. M. Moorwood, *Proc. SPIE*, 4841, 72
- Brimouille, F., Lerchster, M., Seitz, S., Bender, R., & Snigula, J. 2008 [[arXiv:0811.3211](https://arxiv.org/abs/0811.3211)]
- Coleman, G. D., Wu, C.-C., & Weedman, D. W. 1980, *ApJS*, 43, 393
- Coupon, J., Ilbert, O., Kilbinger, M., et al. 2008 [[arXiv:0811.3326](https://arxiv.org/abs/0811.3326)]
- Dahle, H., Pedersen, K., Lilje, P. B., Maddox, S. J., & Kaiser, N. 2003, *ApJ*, 591, 662
- Davis, M., Guhathakurta, P., Konidaris, N. P., et al. 2007, *ApJ*, 660, L1
- Dietrich, J. P., Erben, T., Lamer, G., et al. 2007, *A&A*, 470, 821
- Duda, R. O., & Hart, P. E. 1972, *Commun. ACM*, 15, 11
- Eke, V. R., Cole, S., & Frenk, C. S. 1996, *MNRAS*, 282, 263
- Erben, T., van Waerbeke, L., Mellier, Y., et al. 2000, *A&A*, 355, 23
- Erben, T., Schirmer, M., Dietrich, J. P., et al. 2005, *Astron. Nachr.*, 326, 432
- Feldmann, R., Carollo, C. M., Porciani, C., et al. 2006, *MNRAS*, 372, 565
- Fu, L., Semboloni, E., Hoekstra, H., et al. 2008, *A&A*, 479, 9
- Gal, R. R. 2008, in *Lecture Notes in Physics* (Berlin, Heidelberg: Springer), 740, 119
- Garilli, B., Le Fèvre, O., Guzzo, L., et al. 2008, *A&A*, 486, 683
- Gladders, M. D., & Yee, H. K. C. 2000, *AJ*, 120, 2148
- Gladders, M. D., Yee, H. K. C., Majumdar, S., et al. 2007, *ApJ*, 655, 128
- Goto, T., Sekiguchi, M., Nichol, R. C., et al. 2002, *AJ*, 123, 1807
- Greisen, E. W., & Calabretta, M. R. 2002, *A&A*, 395, 1061
- Gwyn, S. D. J. 2008, *PASP*, 120, 212
- Hetterscheidt, M., Erben, T., Schneider, P., et al. 2005, *A&A*, 442, 43
- Hildebrandt, H., Erben, T., Dietrich, J. P., et al. 2006, *A&A*, 452, 1121
- Hildebrandt, H., Wolf, C., & Benítez, N. 2008, *A&A*, 480, 703
- Hoekstra, H., Mellier, Y., van Waerbeke, L., et al. 2006, *ApJ*, 647, 116
- Huterer, D., Takada, M., Bernstein, G., & Jain, B. 2006, *MNRAS*, 366, 101
- Ilbert, O., Arnouts, S., McCracken, H. J., et al. 2006, *A&A*, 457, 841
- Kerscher, M., Szapudi, I., & Szalay, A. S. 2000, *ApJ*, 535, L13
- Kinney, A. L., Calzetti, D., Bohlin, R. C., et al. 1996, *ApJ*, 467, 38
- Koch, A., Grebel, E., Odenkirchen, M., & Caldwell, J. A. R. 2004, *AN*, 325, 299
- Koester, B. P., McKay, T. A., Annis, J., et al. 2007, *ApJ*, 660, 239
- Landy, S. D., & Szalay, A. S. 1993, *ApJ*, 412, 64
- Le Fèvre, O., Vettolani, G., Garilli, B., et al. 2005, *A&A*, 439, 845
- Lilly, S. J., Le Fèvre, O., Crampton, D., Hammer, F., & Tresse, L. 1995, *ApJ*, 455, 50
- Magnier, E. A., & Cuillandre, J.-C. 2004, *PASP*, 116, 449
- Mandelbaum, R., Seljak, U., Hirata, C. M., et al. 2008, *MNRAS*, 386, 781
- Manfroid, J., Selman, F., & Jones, H. 2001, *ESO Messenger*, 102, 16
- Mantz, A., Allen, S. W., Ebeling, H., & Rapetti, D. 2008, *MNRAS*, 387, 1179
- Marmo, C., & Bertin, E. 2008, in *Astronomical Data Analysis Software and Systems XVII*, ed. R. W. Argyle, P. S. Bunclark, & J. R. Lewis, *ASP Conf. Ser.*, 394, 619
- McCracken, H. J., Radovich, M., Bertin, E., et al. 2003, *A&A*, 410, 17
- Miller, C. J., Nichol, R. C., Reichart, D., et al. 2005, *AJ*, 130, 968
- Mobasher, B., Idzi, R., Benítez, N., et al. 2004, *ApJ*, 600, L167
- Monet, D. G., Levine, S. E., Canzian, B., et al. 2003, *AJ*, 125, 984
- Olsen, L. F., Scodreggio, M., da Costa, L., et al. 1999, *A&A*, 345, 681
- Olsen, L. F., Benoist, C., da Costa, L., et al. 2001, *A&A*, 380, 460
- Pickles, A. J. 1998, *PASP*, 110, 863
- Postman, M., Lubin, L. M., Gunn, J. E., et al. 1996, *AJ*, 111, 615
- Radovich, M. 2002, *ASTROMETRIX User's manual*
- Ramella, M., Boschin, W., Fadda, D., & Nonino, M. 2001, *A&A*, 368, 776
- Regnault, N. 2007, in *The Future of Photometric, Spectrophotometric and Polarimetric Standardization*, ed. C. Sterken, *ASP Conf. Ser.*, 364, 587
- Reiprich, T. H., & Böhringer, H. 2002, *ApJ*, 567, 716
- Schirmer, M., Erben, T., Schneider, P., et al. 2003, *A&A*, 407, 869
- Schirmer, M., Erben, T., Hetterscheidt, M., & Schneider, P. 2007, *A&A*, 462, 875
- Schneider, P. 1996, *MNRAS*, 283, 837
- Schneider, M., Knox, L., Zhan, H., & Connolly, A. 2006, *ApJ*, 651, 14
- Schuecker, P., Böhringer, H., Collins, C. A., & Guzzo, L. 2003a, *A&A*, 398, 867
- Schuecker, P., Caldwell, R. R., Böhringer, H., et al. 2003b, *A&A*, 402, 53
- van Waerbeke, L., White, M., Hoekstra, H., & Heymans, C. 2006, *Astropart. Phys.*, 26, 91
- Vandame, B. 2001, in *Mining the Sky: Proceedings of the MPA/ESO/MPE Workshop Held at Garching, Germany, July 31–August 4, 2000*, *ESO ASTROPHYSICS SYMPOSIA*, 595
- Wittman, D., Tyson, J. A., Margoniner, V. E., et al. 2001, *ApJ*, 557, 89
- Wittman, D., Margoniner, V. E., Tyson, J. A., et al. 2003, *ApJ*, 597, 218
- Wittman, D., Dell'Antonio, I. P., Hughes, J. P., et al. 2006, *ApJ*, 643, 128